INTERNATIONAL JOURNAL FOR NUMERICAL METHODS IN ENGINEERING
Int. J. Numer. Meth. Engng (2008)
Published online in Wiley InterScience (www.interscience.wiley.com). DOI: 10.1002/nme.2421

Upper and lower bounds in limit analysis: Adaptive meshing strategies and discontinuous loading

J. J. Muñoz[1,*,†], J. Bonet[2], A. Huerta[1] and J. Peraire[3]

[1]*Dep. Applied Mathematics III, LaCàN, Univ. Poitècnica de Catalunya (UPC), Barcelona, Spain*
[2]*Civil and Computational Engineering Centre, School of Engineering, University of Wales, Swansea, U.K.*
[3]*Department of Aeronautics and Astronautics, Massachusetts Institute of Technology, U.S.A.*

SUMMARY

Upper and lower bounds of the collapse load factor are here obtained as the optimum values of two discrete constrained optimization problems. The membership constraints for Von Mises and Mohr–Coulomb plasticity criteria are written as a set of quadratic constraints, which permits one to solve the optimization problem using specific algorithms for Second-Order Conic Program (SOCP). From the stress field at the lower bound and the velocities at the upper bound, we construct a novel error estimate based on elemental and edge contributions to the bound gap. These contributions are employed in an adaptive remeshing strategy that is able to reproduce fan-type mesh patterns around points with discontinuous surface loading. The solution of this type of problems is analysed in detail, and from this study some additional meshing strategies are also described. We particularise the resulting formulation and strategies to two-dimensional problems in plane strain and we demonstrate the effectiveness of the method with a set of numerical examples extracted from the literature. Copyright © 2008 John Wiley & Sons, Ltd.

Received 26 September 2007; Revised 5 May 2008; Accepted 7 June 2008

KEY WORDS: limit analysis; bounds; adaptive remeshing; optimization

1. INTRODUCTION

The computation of load estimates for limit analysis has relied traditionally on practitioners' experience and a catalogue of solutions for simple academic cases. Although these solutions are

*Correspondence to: J. J. Muñoz, Dep. Applied Mathematics III, LaCàN, Univ. Poitècnica de Catalunya (UPC), Barcelona, Spain.
†E-mail: j.munoz@upc.edu, http://www-lacan.upc.es

Contract/grant sponsor: Spanish Ministry of Education and Science (MEC)
Contract/grant sponsor: Juan de la Cierva; contract/grant number: BIA2007-66965

well founded in the lower and upper bound theorems of limit analysis [1, 2], it is still desirable to develop general methods that can be applied to a broader number of practical problems. Early numerical methods for limit analysis were developed more than 30 years ago [3, 4], but more recently these problems have gained increasing attention (see, for instance, References [2, 5–8]). This is partly due to the development of the robust optimization methods on which they strongly rely and recent progress in the computation of bounds [7–10].

In the present paper, we compute upper and lower bounds of the load factor. This is achieved by constructing a set of purely static and kinematic interpolation spaces of the velocities and stresses, which are analogous to those given in [9–12]. The discretizations for the lower bound problem are also the same as those described in [7, 8]. We write the upper and lower bound optimization problems as a function of the stresses, which are considered the primal variables. We note that each one of the optimization problems can be stated as a function of the velocities (dual variables), and examples of the latter case may be found in the literature [13].

The solution of the constrained optimization problem is found resorting to Second-Order Conic Programming (SOCP). We have used the general packages for conic programming SeDuMi [14] and SDPT3 [15], which are embedded in Matlab. Other specific programs for SOCP such as MOSEK [16] have also been recently used in the context of limit analysis [8]. This is in contrast to the usual methodology, where the bounds are computed resorting to non-linear programming (NLP) [5–7, 13, 17–20]. However, the latter requires a twice differentiable boundary of the yield surface, i.e. no apex as in the Mohr–Coulomb or Drucker–Prager criteria. In these cases, NLP requires the smoothing of the criteria or the linearization of the yield surfaces in order to solve the constraints [13, 17]. In contrast, SOCP does not require any modification of the admissibility plastic domains, as long as they can be written as a second-order cone, which is the case in the usual two-dimensional plastic models such as Mohr–Coulomb, Von Mises or Tresca. In three-dimensional analysis, although Drucker–Prager or Von Mises criteria are expressible as second-order cones, the membership constraints of other common plasticity models such as Tresca, Mohr–Coulomb or Hoek–Brown are semidefinite cones [21]. This is due to the fact that the latter depend on the maximum or minimum values of the principal stresses, and not on the first or second invariants. Consequently, these cases do not belong to SOCP, and cannot exploit the approach used here. We restrict here our study to plane strain two-dimensional cases, in conjunction with Von Mises and Mohr–Coulomb plasticity, although the formulation given here can also be written for plane stress problems [9, 10] or generalized to three-dimensional problems.

Owing to the presence of large areas that remain practically rigid, there is a strong need for the employment of an adaptive remeshing strategy. Since no *a priori* error estimates for limit analysis exist, the usual approach is to use *a posteriori* techniques, such as non-zero strain rates and the proximity of the stresses to the yield surface [20], or alternatively the recovery of a Hessian matrix in order to provide an anisotropic error estimates [5, 18, 22]. We employ here an error estimate, which is constructed from the combined solution of the lower and upper bound problem, and thus benefits from the dual structure of limit analysis. Our *a posteriori* error estimate is an extension of the one employed in [9–12], due to an additional term corresponding to the contributions of the internal edges.

The resulting error estimate is able to avoid the locking of the lower bound in the presence of discontinuous loading (as it is often the case in strip footings or foundation slabs). Alternatively, we also suggest a strategy that remeshes around nodes according to the values of the velocities at the internal edges. A similar criterion has been suggested in [18]. However, we describe here a strategy that constructs fan-type meshes with subdivisions only in the necessary directions. The

DOI: 10.1002/nme

need for fan-type patterns has been already pointed out in [1, 7, 8, 18]. In Section 5 we analyse the source of the locking phenomena when no fans are used in the discretized problem, which interestingly shows that the limit load factor of the continuum problem is in fact governed by a local problem at the point of the load discontinuity.

We compare our formulation with a set of problems extracted from the literature [7, 8, 17, 18, 22–24]. We show that our remeshing strategies can improve the bounds given by previous formulations using a similar number of elements.

2. DUALITY AND BOUNDS IN LIMIT ANALYSIS

Let us consider a rigid-plastic body $\Omega \subset \mathbb{R}^2$, where the stress field $\boldsymbol{\sigma}$ is constrained to belong to the domain

$$\mathscr{B} = \{\boldsymbol{\sigma} | f(\boldsymbol{\sigma}) \leqslant 0\}$$

with $f(\boldsymbol{\sigma})$ the so-called yield function. In two-dimensional plane strain Von Mises and Mohr–Coulomb plasticity, it is, respectively, given by

$$f(\boldsymbol{\sigma})_{\mathrm{VM}} = \sqrt{(\sigma_{xx} - \sigma_{yy})^2 + 4\sigma_{xy}^2} - \frac{2}{\sqrt{3}}\sigma_Y$$

$$f(\boldsymbol{\sigma})_{\mathrm{MC}} = \sqrt{(\sigma_{xx} - \sigma_{yy})^2 + 4\sigma_{xy}^2} + (\sigma_{xx} + \sigma_{yy}) \sin\phi - 2c\cos\phi$$

where σ_Y is the yield stress at simple tension, and c and ϕ are the soil cohesion and internal friction angle, respectively. In general, we require the following assumptions on the set $\mathscr{B}$:

- $\exists \varepsilon > 0$, such that if $\sum_{i,j} |\sigma_{ij}| < \varepsilon \Rightarrow \boldsymbol{\sigma} \in \mathscr{B}$ (the zero stress state belongs to $\mathscr{B}$).
- The set $\mathscr{B}$ is convex and closed.

In this work we restrict our attention to bodies subjected to variable loads. These are given by the body load $\lambda \mathbf{f}$ at the interior of Ω and the surface load $\lambda \mathbf{g}$ at Γ_g. In addition, homogeneous Dirichlet boundary conditions are also applied at Γ_u, with $\Gamma_g \cap \Gamma_u = \emptyset$ and $\Gamma_g \cup \Gamma_u = \partial\Omega$. The objective of the limit analysis is to determine the value of the load factor λ at which the domain Ω collapses. This value will be denoted by λ^*.

We note that due to the rigid-plastic assumption, and thus in contrast to elastic materials, no constitutive relation exists between the strain rate tensor[‡] $\varepsilon(\mathbf{u}) = \frac{1}{2}(\nabla\mathbf{u} + (\nabla\mathbf{u})^{\mathrm{T}})$ and the stress tensor $\boldsymbol{\sigma}$. Both variables are related through the associative plasticity rule $\varepsilon = \gamma \partial f(\boldsymbol{\sigma})/\partial\boldsymbol{\sigma}$, where γ is the plastic multiplier. We henceforth denote the spaces for the stress and velocity field by $\Sigma \ni \boldsymbol{\sigma}$ and $\mathscr{U} \ni \mathbf{u}$, respectively. The smooth requirements for Σ and $\mathscr{U}$ that guarantee the existence of solutions can be found, for instance, in [2].

[‡]We denote the *velocity* and strain *rates* by $\mathbf{u}$ and $\varepsilon(\mathbf{u})$, respectively.

DOI: 10.1002/nme

2.1. Lower bound theorem

The lower bound theorem of limit analysis can be stated as follows [1]:

> *If for a given load factor* $\tilde{\lambda}$ *the stress field* (*i*) *satisfies the stress boundary conditions*, (*ii*) *is in static equilibrium and* (*iii*) *does not violate the yield condition*, *then the load factor is a lower bound of the collapse load*, *i.e.* $\tilde{\lambda} \leqslant \lambda^*$.

The boundary equilibrium condition in (i) is given by $\boldsymbol{\sigma}\mathbf{n} = \lambda \mathbf{g}$ at Γ_g, with $\mathbf{n}$ being the unit external normal. This condition and the enforcement of (ii) imply that the work rate of the external loads is equal to the internal energy rate, which can expressed as follows:

$$a(\boldsymbol{\sigma}, \mathbf{u}) = \lambda \ell(\mathbf{u}) \quad \forall \mathbf{u} \in \mathscr{U}$$

The bilinear and linear forms $a(,)$ and $\ell()$ have the usual expressions

$$a(\boldsymbol{\sigma}, \mathbf{u}) = \int_\Omega \boldsymbol{\sigma} : \varepsilon(\mathbf{u}) \, \mathrm{d}V \tag{1a}$$

$$\ell(\mathbf{u}) = \int_\Omega \mathbf{f} \cdot \mathbf{u} \, \mathrm{d}V + \int_{\Gamma_g} \mathbf{u} \cdot \mathbf{g} \, \mathrm{d}\Gamma \tag{1b}$$

It follows that, according to the lower bound theorem, the collapse load factor λ^* can be found by solving the following optimization problem:

$$\lambda^* = \sup_{\substack{\lambda, \boldsymbol{\sigma} \in \mathscr{B} \\ a(\boldsymbol{\sigma}, \mathbf{u}) = \lambda \ell(\mathbf{u}), \ \forall \mathbf{u} \in \mathscr{U}}} \lambda \tag{2}$$

From the expressions of $a(,)$ and $\ell()$ in (1), and after integrating by parts $a(,)$, we have that $a(\boldsymbol{\sigma}, \mathbf{u}) - \lambda \ell(\mathbf{u}) = -\int (\nabla \cdot \boldsymbol{\sigma} + \lambda \mathbf{f}) \cdot \mathbf{u} \, \mathrm{d}V$, if the boundary equilibrium condition holds. Therefore, from the linearity of this expression in $\mathbf{u}$, we can express

$$\inf_{\mathbf{u}} a(\boldsymbol{\sigma}, \mathbf{u}) - \lambda \ell(\mathbf{u}) = \begin{cases} 0 & \text{if } a(\boldsymbol{\sigma}, \mathbf{u}) = \lambda \ell(\mathbf{u}) \ \forall \mathbf{u} \in \mathscr{U} \\ -\infty & \text{otherwise} \end{cases} \tag{3}$$

Consequently, we can express λ^* in (2) as

$$\lambda^* = \sup_{\lambda, \boldsymbol{\sigma} \in \mathscr{B}} \inf_{\mathbf{u}} (a(\boldsymbol{\sigma}, \mathbf{u}) + \lambda(1 - \ell(\mathbf{u}))) = \sup_{\boldsymbol{\sigma} \in \mathscr{B}} \inf_{\ell(\mathbf{u}) = 1} a(\boldsymbol{\sigma}, \mathbf{u}) \tag{4}$$

where the last identity follows from the fact that λ is a free variable.

2.2. Upper bound theorem

Let us introduce the internal rate of dissipation $D(\mathbf{u})$ as

$$D(\mathbf{u}) = \sup_{\boldsymbol{\sigma} \in \mathscr{B}} \int_\Omega \boldsymbol{\sigma} : \varepsilon(\mathbf{u}) \, \mathrm{d}V = \sup_{\boldsymbol{\sigma} \in \mathscr{B}} a(\boldsymbol{\sigma}, \mathbf{u}) \tag{5}$$

From the associative plasticity rule, $D(\mathbf{u})$ may be expressed via the parameters in the yield function $f(\boldsymbol{\sigma})$, and an equivalent strain rate, $\varepsilon_{\mathrm{eq}}(\mathbf{u}) = \sqrt{2\varepsilon(\mathbf{u}) : \varepsilon(\mathbf{u})/3}$. Expressions for $D(\mathbf{u})$ in Von Mises and two-dimensional Mohr–Coulomb plasticity can be found in Appendix A.

DOI: 10.1002/nme

With definition (5) at hand, the upper bound theorem of limit analysis can be stated as follows [1]:

Those loads determined by equating the external rate of work and the internal rate of dissipation in an assumed velocity field, which satisfies (*i*) *the Dirichlet boundary conditions and* (*ii*) *strain and velocity compatibility conditions* ($2\varepsilon(\mathbf{u})=\frac{1}{2}(\nabla\mathbf{u}+(\nabla\mathbf{u})^{\mathrm{T}})$ and $\mathbf{u}=0$ at Γ_u), *are not less than the collapse load.*

Therefore, according to the upper load theorem, the collapse load factor may be computed as

$$\lambda^*=\inf_{D(\mathbf{u})=\lambda\ell(\mathbf{u})}\lambda=\inf_{\mathbf{u}}\frac{D(\mathbf{u})}{\ell(\mathbf{u})}=\inf_{\ell(\mathbf{u})=1}D(\mathbf{u})=\inf_{\ell(\mathbf{u})=1}\sup_{\boldsymbol{\sigma}\in\mathscr{B}}a(\boldsymbol{\sigma},\mathbf{u}) \tag{6}$$

2.3. Duality and load factor bounds λ^{LB} and λ^{UB}

Both identities (4) and (6) unveil the structure of limit analysis: the optimum values $(\lambda^*,\boldsymbol{\sigma}^*,\mathbf{u}^*)$ are the solution of the saddle point problem in (4) and (6), which satisfy $a(\boldsymbol{\sigma}^*,\mathbf{u}^*)=\lambda^*$ in the domain $\mathscr{B}\times\mathscr{C}\times\mathbb{R}\ni(\boldsymbol{\sigma},\mathbf{u},\lambda)$, with $\mathscr{C}=\{\mathbf{u}|\ell(\mathbf{u})=1\}$. This fact permits one to compute bounds of the collapse load factor λ^*. Assuming that the set $\mathscr{B}\ni\boldsymbol{\sigma}$ is convex, and since the objective function $a(\boldsymbol{\sigma},\mathbf{u})$ and the constraint $\ell(\mathbf{u})=1$ are linear (and therefore also convex), strong duality holds [25], which means that the optimum values λ^* in (4) and (6) are the same if they exist (see [2] for existence conditions). Bounds of the collapse load factor may then be computed using the following relations:

$$\lambda^{\mathrm{LB}}=a(\boldsymbol{\sigma},\mathbf{u}^*)\leqslant\lambda^*=a(\boldsymbol{\sigma}^*,\mathbf{u}^*)\leqslant a(\boldsymbol{\sigma}^*,\mathbf{u})=\lambda^{\mathrm{UB}} \tag{7}$$

These inequalities are satisfied for the spaces Σ and $\mathscr{U}$ describing the continuum fields $\boldsymbol{\sigma}$ and $\mathbf{u}$, respectively. We next introduce a set of discrete spaces Σ^h and $\mathscr{U}^h$ that preserve the validity of the two inequalities in (7). These spaces are the same as those given in [9, 10], but are here recast in order to introduce the necessary tools that will be employed in subsequent sections.

3. LOWER BOUND PROBLEM

Discrete spaces $\Sigma^{\mathrm{LB}}\ni\boldsymbol{\sigma}^{\mathrm{LB}}$ and $\mathscr{U}^{\mathrm{LB}}\ni\mathbf{u}^{\mathrm{LB}}$ that ensure the first inequality in (7) will be termed *purely static spaces*. These must therefore satisfy the following relation:

$$\max_{\boldsymbol{\sigma}^{\mathrm{LB}}\in\mathscr{B}^{\mathrm{LB}}}\min_{\ell(\mathbf{u}^{\mathrm{LB}})=1}a(\boldsymbol{\sigma}^{\mathrm{LB}},\mathbf{u}^{\mathrm{LB}})\leqslant\sup_{\boldsymbol{\sigma}\in\mathscr{B}}\inf_{\ell(\mathbf{u})=1}a(\boldsymbol{\sigma},\mathbf{u}) \tag{8}$$

The set of admissible discrete stresses, $\mathscr{B}^{\mathrm{LB}}$, is determined below. Following a similar reasoning to (3), condition (8) is equivalent to

$$\max_{\lambda,\boldsymbol{\sigma}^{\mathrm{LB}}\in\mathscr{B}^{\mathrm{LB}}}\left(\lambda+\min_{\mathbf{u}^{\mathrm{LB}}}a(\boldsymbol{\sigma}^{\mathrm{LB}},\mathbf{u}^{\mathrm{LB}})-\lambda\ell(\mathbf{u}^{\mathrm{LB}})\right)\leqslant\sup_{\lambda,\boldsymbol{\sigma}\in\mathscr{B}}\left(\lambda+\inf_{\mathbf{u}}a(\boldsymbol{\sigma},\mathbf{u})-\lambda\ell(\mathbf{u})\right)$$

This relation is satisfied if the following three conditions hold:

$$a(\boldsymbol{\sigma}^{\mathrm{LB}},\mathbf{u}^{\mathrm{LB}})=\lambda\ell(\mathbf{u}^{\mathrm{LB}})\quad\forall\mathbf{u}^{\mathrm{LB}}\in\mathscr{U}^{\mathrm{LB}}\Rightarrow a(\boldsymbol{\sigma}^{\mathrm{LB}},\mathbf{u})=\lambda\ell(\mathbf{u}),\ \forall\mathbf{u}\in\mathscr{U} \tag{9a}$$

$$\mathscr{B}^{\mathrm{LB}}\subseteq\mathscr{B} \tag{9b}$$

$$\boldsymbol{\sigma}^{\mathrm{LB}}\in\mathscr{B}^{\mathrm{LB}}\text{ at discrete points}\Rightarrow\boldsymbol{\sigma}^{\mathrm{LB}}\in\mathscr{B}^{\mathrm{LB}}\text{ everywhere} \tag{9c}$$

DOI: 10.1002/nme

A pair of spaces that satisfy these conditions can be constructed as follows. We first discretize the domain with *nele* three-noded triangles and using a triangulation $\mathscr{T}_h(\Omega)$. The stress and velocity fields are then interpolated in the following manner (see [9, 10]):

- Σ^{LB}: Piecewise linear stress field interpolated from the nodal values $\boldsymbol{\sigma}^{n,e}$, $n=1,2,3; e=1,\ldots,nele$, with a set of complete Lagrangian functions I^n, i.e. $\sum_n I^n = 1$. Each element has a distinct set of nodes, and thus discontinuities at each elemental boundary $\xi^{e-e'}$ (between elements e and e') are permitted.
- $\mathscr{U}^{\mathrm{LB}}$: Constant velocities at each element e. Additionally, a linear velocity field is introduced at each interior edge $\xi^{e-e'}$ and external edge ξ_e.

These spaces are depicted in Figure 1. In addition, we impose the stress admissibility condition to the nodal stress values, i.e. $\boldsymbol{\sigma}^{n,e} \in \mathscr{B}$, $\forall n=1,2,3, e=1,\ldots,nele$, or in other words, $\mathscr{B}^{\mathrm{LB}} = \{\boldsymbol{\sigma}^{\mathrm{LB}} | \boldsymbol{\sigma}^{n,e} \in \mathscr{B}\ \forall n,e\}$. Since the interpolating functions are complete, and $\mathscr{B}$ is convex, we have that conditions (9b) and (9c) hold, and $\boldsymbol{\sigma}^{\mathrm{LB}} \in \mathscr{B}$, $\forall \boldsymbol{\sigma}^{\mathrm{LB}} \in \Sigma^{\mathrm{LB}}$ at all points of the discretized Ω. The lower bound λ^{LB} is computed recalling the lower bound theorem, in particular, Equation (2) in terms of the discrete spaces given above:

$$\lambda^{\mathrm{LB}} = \max_{\substack{\lambda, \boldsymbol{\sigma}^{\mathrm{LB}} \in \mathscr{B}^{\mathrm{LB}} \\ a(\boldsymbol{\sigma}^{\mathrm{LB}}, \mathbf{u}^{\mathrm{LB}}) = \lambda \ell(\mathbf{u}^{\mathrm{LB}}),\ \forall \mathbf{u}^{\mathrm{LB}} \in \mathscr{U}^{\mathrm{LB}}}} \lambda \tag{10}$$

When using the discrete spaces $\boldsymbol{\sigma}^{\mathrm{LB}}$ and $\mathbf{u}^{\mathrm{LB}}$ in the expression of $a(,)$, and noting that $\mathbf{u}^{\mathrm{LB}}$ is piecewise constant, the problem in (10) may be expressed as

$$\lambda^{\mathrm{LB}} = \max \quad \lambda$$
$$\text{s.t.} \quad \begin{cases} \nabla \cdot \boldsymbol{\sigma}^{\mathrm{LB}} + \lambda \mathbf{f} = \mathbf{0} \\ \boldsymbol{\sigma}^{\mathrm{LB}} \mathbf{n} = \lambda \mathbf{g} \quad \text{at } \Gamma_g \\ (\boldsymbol{\sigma}_e^{\mathrm{LB}} - \boldsymbol{\sigma}_{e'}^{\mathrm{LB}}) \mathbf{n}^{e-e'} = \mathbf{0} \\ \boldsymbol{\sigma}^{\mathrm{LB}} \in \mathscr{B}^{\mathrm{LB}} \end{cases} \tag{11}$$

Since Equations (11) are in fact the equilibrium equations of the continuum, condition (9a) also holds, and therefore, the spaces Σ^{LB} and $\mathscr{U}^{\mathrm{LB}}$ are purely static.

It is shown in Appendix B that, after making use of the interpolation spaces and assembling the equilibrium and boundary conditions, the optimization problem in (11), for Von Mises or

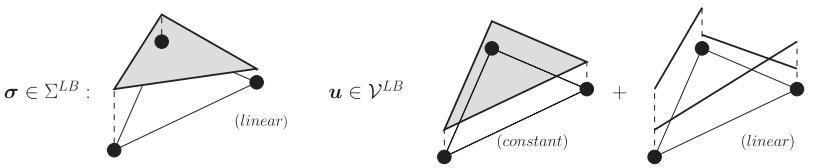

Figure 1. Scheme of the lower bound discrete spaces Σ^{LB} and $\mathscr{U}^{\mathrm{LB}}$ used for the stresses and velocities, respectively.

DOI: 10.1002/nme

Mohr–Coulomb plasticity with $\phi=0$, can be expressed in the following form:

$$\begin{aligned}
&\max \quad \lambda \\
&\text{s.t.} \quad \begin{cases}
\begin{bmatrix} \mathbf{f} & \mathbf{0} & \mathbf{A}_M \\ \mathbf{g} & \mathbf{0} & \mathbf{N}_M^g \\ \mathbf{0} & \mathbf{0} & \mathbf{N}_M^{e-e'} \\ \mathbf{0} & \mathbf{I} & \mathbf{0} \end{bmatrix} \begin{Bmatrix} \lambda \\ \mathbf{x}_1^{\mathrm{LB}} \\ \mathbf{x}_{24}^{\mathrm{LB}} \end{Bmatrix} = \begin{Bmatrix} \mathbf{0} \\ \mathbf{0} \\ \mathbf{0} \\ \mathbf{b} \end{Bmatrix} \\
\mathbf{x}_4^{\mathrm{LB}}, \quad \lambda \text{ free} \\
\mathbf{x}_{13}^{\mathrm{LB}} \in \underbrace{\mathscr{L}^3 \times \cdots \times \mathscr{L}^3}_{3\times nele}
\end{cases}
\end{aligned}$$

For Mohr–Coulomb plasticity with $\phi\neq 0$, the following expression is obtained instead:

$$\begin{aligned}
&\max \quad \lambda \\
&\text{s.t.} \quad \begin{cases}
\begin{bmatrix} \mathbf{f} & \mathbf{A}_M \\ \mathbf{g} & \mathbf{N}_M^g \\ \mathbf{0} & \mathbf{N}_M^{e-e'} \end{bmatrix} \begin{Bmatrix} \lambda \\ \mathbf{x}_{13}^{\mathrm{LB}} \end{Bmatrix} = \begin{Bmatrix} -\mathbf{d}_{AM} \\ -\mathbf{d}_{NM} \\ \mathbf{0} \end{Bmatrix} \\
\lambda \text{ free} \\
\mathbf{x}_{13}^{\mathrm{LB}} \in \underbrace{\mathscr{L}^3 \times \cdots \times \mathscr{L}^3}_{3\times nele}
\end{cases}
\end{aligned}$$

Explicit expressions of matrices $\mathbf{A}_M$, $\mathbf{N}_M^g$ and $\mathbf{N}_M^{e-e'}$ and vectors $\mathbf{d}_{AM}$ and $\mathbf{d}_{NM}$ are also given in Appendix B. The variables $\mathbf{x}^{\mathrm{LB}}$, which are a linear transformation of the stresses $\boldsymbol{\sigma}^{\mathrm{LB}}$, have been introduced in order to express the yield surface as a product of second-order cones (also named Lorentz or quadratic cones) $\mathscr{L}^3=\{\mathbf{x}\in\mathbb{R}^3 | x_1 \geqslant \sqrt{x_2^2+x_3^2}\}$.

The resulting optimization problem is highly sparse and has the standard form of an SOCP. Specific techniques for such problems have been developed recently, and in particular, we have used SeDuMi [14] and SDPT3 [15] with satisfactory results, as the numerical examples in Section 7 show.

4. UPPER BOUND PROBLEM

Discrete spaces $\Sigma^{\mathrm{UB}} \ni \boldsymbol{\sigma}^{\mathrm{UB}}$ and $\mathscr{U}^{\mathrm{UB}} \ni \mathbf{u}^{\mathrm{UB}}$ that preserve the second inequality in (7) will be termed *purely kinematic spaces*. These spaces must then satisfy

$$\sup_{\boldsymbol{\sigma}\in\mathscr{B}} a(\boldsymbol{\sigma},\mathbf{u}) \leqslant \max_{\boldsymbol{\sigma}^{\mathrm{UB}}\in\mathscr{B}^{\mathrm{UB}}} a(\boldsymbol{\sigma}^{\mathrm{UB}},\mathbf{u}^{\mathrm{UB}}) \quad \forall \mathbf{u}^{\mathrm{UB}}\in\Sigma^{\mathrm{UB}} \tag{12}$$

We will next describe a set of purely kinematic spaces and demonstrate their kinematic nature, which depends on the definition of the set of admissible stresses $\mathscr{B}^{\mathrm{UB}}$.

DOI: 10.1002/nme

We resort to the same triangulation $\mathscr{T}_h(\Omega)$ employed in the lower problem. However, the discrete stress and velocity fields are now given by [9, 10] (see Figure 2):

- Σ^{UB}: A piecewise constant stress field $\boldsymbol{\sigma}^{\mathrm{UB}}$ at each element e is considered, which is in general discontinuous at the element edges. In addition, we introduce a traction field $\mathbf{t}^{\mathrm{UB}}$ defined at each internal edge $\xi^{e-e'}$.
- $\mathscr{U}^{\mathrm{UB}}$: Piecewise linear velocities at each element e, which are also discontinuous at the element edges.

Owing to the presence of the traction field, an additional set of admissible tractions $\mathscr{B}_t^{\mathrm{UB}}$ must be defined in such a way that the kinematic nature of the spaces is not violated. This set will be determined below.

By using the results of the upper bound theorem in (6), with the discrete spaces that preserve relation (12), we can compute the upper bound of the load factor λ^{UB} as the solution of the following optimization problem:

$$\lambda^{\mathrm{UB}} = \min_{\ell(\mathbf{u}^{\mathrm{UB}})=1} \max_{\substack{\boldsymbol{\sigma}^{\mathrm{UB}}\in\mathscr{B}^{\mathrm{UB}} \\ \mathbf{t}^{\mathrm{UB}}\mathscr{B}_t^{\mathrm{UB}}}} a((\boldsymbol{\sigma}^{\mathrm{UB}}, \mathbf{t}^{\mathrm{UB}}), \mathbf{u}^{\mathrm{UB}}) \tag{13a}$$

$$= \max \quad \lambda$$

$$\text{s.t.} \quad \begin{cases} a((\boldsymbol{\sigma}^{\mathrm{UB}}, \mathbf{t}^{\mathrm{UB}}), \mathbf{u}^{\mathrm{UB}}) = \lambda \ell(\mathbf{u}^{\mathrm{UB}}) \\ \boldsymbol{\sigma}^{\mathrm{UB}} \in \mathscr{B}^{\mathrm{UB}} \\ \mathbf{t}^{\mathrm{UB}} \in \mathscr{B}_t^{\mathrm{UB}} \end{cases} \tag{13b}$$

where the last identity follows resorting to a reasoning analogous to the one used when deriving equations (2)–(4). Owing to the presence of the edge tractions $\mathbf{t}^{\mathrm{UB}}$, the internal rate of dissipation has an additional term that accounts for the dissipation at the internal edges, i.e.

$$a((\boldsymbol{\sigma}^{\mathrm{UB}}, \mathbf{t}^{\mathrm{UB}}), \mathbf{u}^{\mathrm{UB}}) = \sum_{e=1}^{nele} \int_{\Omega^e} \boldsymbol{\sigma}^{\mathrm{UB}} : \varepsilon(\mathbf{u}^{\mathrm{UB}})\, \mathrm{d}V + \sum_{\xi^{e-e'}=1}^{N_I} \int_{\xi^{e-e'}} \mathbf{t}^{\mathrm{UB}} \cdot [\![\mathbf{u}^{\mathrm{UB}}]\!]\, \mathrm{d}\Gamma \tag{14}$$

where $[\![\mathbf{u}^{\mathrm{UB}}]\!] = \mathbf{u}^{UB,e} - \mathbf{u}^{UB,e'}$ and N_I is the number of internal edges. The purely kinematic nature of the spaces Σ^{UB} and $\mathscr{U}^{\mathrm{UB}}$ defined above has been proved in [9, 10] for Von Mises plasticity and for a particular set of admissible tractions $\mathscr{B}_t^{\mathrm{UB}}$. We will also construct a set of admissible tractions for Mohr–Coulomb plasticity and show that the spaces Σ^{UB} and $\mathscr{U}^{\mathrm{UB}}$ preserve their kinematic nature.

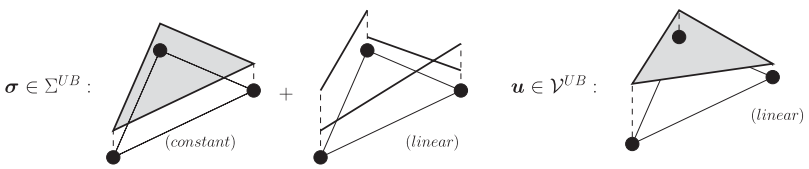

Figure 2. Scheme of the upper bound discrete spaces Σ^{UB} and $\mathscr{U}^{\mathrm{UB}}$ used for the stresses and velocities, respectively.

DOI: 10.1002/nme

Let us first note that since the stress field $\boldsymbol{\sigma}^{\mathrm{UB}}$ is constant and the tractions are linear, the computation of the maximum

$$D(\mathbf{u}^{\mathrm{UB}}) = \max_{\substack{\boldsymbol{\sigma}^{\mathrm{UB}} \in \mathscr{B} \\ \mathbf{t}^{\mathrm{UB}} \in \mathscr{B}_t^{\mathrm{UB}}}} a((\boldsymbol{\sigma}^{\mathrm{UB}}, \mathbf{t}^{\mathrm{UB}}), \mathbf{u}^{\mathrm{UB}})$$

is reached for a linear velocity field, and thus, our choice for $\mathbf{u}^{\mathrm{UB}} \in \mathscr{U}^{\mathrm{UB}}$ will capture exactly such maximum if $\mathscr{B}^{\mathrm{UB}} \equiv \mathscr{B}$, or at least exceeded if

$$\mathscr{B}^{\mathrm{UB}} \supseteq \mathscr{B}$$

We will ensure this relation (i) by imposing the membership $\boldsymbol{\sigma}^{\mathrm{UB}} \in \mathscr{B}$ at the interior of the triangles and, (ii) given a stress tensor at the edges $\boldsymbol{\sigma}_{\xi}^{\mathrm{UB}}$, by defining a set $\mathscr{B}_t^{\mathrm{UB}}$ for the traction field $\mathbf{t}^{\mathrm{UB}} = \boldsymbol{\sigma}_{\xi}^{\mathrm{UB}} \mathbf{n}^{e-e'}$ in such a way that we have

$$\boldsymbol{\sigma}_{\xi}^{\mathrm{UB}} \in \mathscr{B} \Rightarrow \mathbf{t}^{\mathrm{UB}} = \boldsymbol{\sigma}_{\xi}^{\mathrm{UB}} \mathbf{n} \in \mathscr{B}_t^{\mathrm{UB}} \quad \forall \mathbf{n} \tag{15}$$

In parallel with the elemental stress admissibility condition, the set $\mathscr{B}_t^{\mathrm{UB}}$ may be expressed as

$$\mathscr{B}_t^{\mathrm{UB}} = \{\mathbf{t}^{\mathrm{UB}} |\ f_t(\mathbf{t}^{\mathrm{UB}}) \leqslant 0\} \tag{16a}$$

where $f_t(\mathbf{t}^{\mathrm{UB}})$ is the yield functions for tractions, which for Von Mises and Mohr–Coulomb plasticity we define them as

$$f_{t,VM}(\mathbf{t}^{\mathrm{UB}}) = |t_T^{\mathrm{UB}}| - \sigma_Y/\sqrt{3} \tag{16b}$$

$$f_{t,MC}(\mathbf{t}^{\mathrm{UB}}) = |t_T^{\mathrm{UB}}| - c + t_N \tan\phi \tag{16c}$$

with t_T and t_N being the tangent and normal components of $\mathbf{t}^{\mathrm{UB}}$ with respect to the orientation of the edge $\xi^{e-e'}$. It can be verified that indeed, for both cases, condition (15) is satisfied, and hence, for both the internal stresses and the (hypothetical) stresses at the edges, we have $\boldsymbol{\sigma}^{\mathrm{UB}} \in \mathscr{B}$ and $\boldsymbol{\sigma}_{\xi}^{\mathrm{UB}} \in \mathscr{B}^{\mathrm{UB}} \supseteq \mathscr{B}$. It then follows that the spaces Σ^{UB} and $\mathscr{U}^{\mathrm{UB}}$ are purely kinematic.

In Appendix C we turn the upper bound optimization problem in (13b) into a standard SOCP, which is explicitly given in Equations (C5a) and (C5b). We just mention that, like in the lower bound problem, we transform the stresses $(\boldsymbol{\sigma}^{\mathrm{UB}}, \mathbf{t}^{\mathrm{UB}})$ into a set of variables $(\mathbf{x}^{\mathrm{UB}}, \mathbf{z}^{\mathrm{UB}})$ which allow us to recast the membership constraints $\boldsymbol{\sigma}^{\mathrm{UB}} \in \mathscr{B}$ and $\mathbf{t}^{\mathrm{UB}} \in \mathscr{B}_t^{\mathrm{UB}}$ in the form $\mathbf{x}^{\mathrm{UB}} \in \underbrace{\mathscr{L}^3 \times \cdots \times \mathscr{L}^3}_{nele}$ and $\mathbf{z}^{\mathrm{UB}} \in \underbrace{\mathscr{L}^2 \times \cdots \times \mathscr{L}^2}_{N_I}$, respectively.

5. ANALYSIS OF THE LOWER BOUND PROBLEM WITH DISCONTINUOUS SURFACE LOADING

Before introducing the adaptive remeshing strategies, we will here analyse a locking effect that occurs when a discontinuous surface loading is applied. The conclusions derived here will help us to design an effective remeshing strategy in Section 6.

DOI: 10.1002/nme

The need for fan-type mesh distribution around points with discontinuous Neumann conditions was already pointed out by Chen [1] when analysing the strip footing problem with the lower bound theorem and adding discontinuities in the stress field. These discontinuities allow variations in the direction of the principal stress when using elements with constant stresses. This fact was recognized in [1] when subdividing the rigid-plastic domain into subdomains that are in static equilibrium, and also in the context of the discretizations of the stress and velocity fields used [7, 8]. The usual approach for such situations is to use a large number of fan-type elements around the point with the load discontinuity.

In order to study the necessity for this mesh pattern, we first analyse the simple problem depicted in Figure 3(a), which we will solve using the lower bound formulation given in Section 3. The vertical surface load $\mathbf{g}^{\mathrm{T}}=\{0,-1\}$ is applied along a free surface, with a discontinuity at point P. The domain around P is discretized first with two elements, a and b, which are connected at point P at the nodes also denoted by a and b (see Figure 3(b)). The maximum load factor obtained for this local system considered here is denoted by λ^{loc}. According to the discretized lower bound problem, the stress is piecewise linear, and thus discontinuity is allowed at the top Neumann boundaries (with normal vectors $\mathbf{n}^1$ and $\mathbf{n}^3$) and at the vertical internal edge (with normal vector $\mathbf{n}^2$). However, in order to guarantee a rigorous lower bound, equilibrium is enforced at these boundaries, or equivalently, due to the linearity of the stress field, at nodes a and b. Consequently, the following nodal equilibrium equations are obtained:

$$\begin{aligned}\boldsymbol{\sigma}^a\mathbf{n}^1&=\lambda^{\mathrm{loc}}\mathbf{g}\\(\boldsymbol{\sigma}^a-\boldsymbol{\sigma}^b)\mathbf{n}^2&=\mathbf{0}\\\boldsymbol{\sigma}^b\mathbf{n}^3&=\mathbf{0}\end{aligned}\tag{17}$$

It can be verified that the previous equations allow one to express the stresses at a and b as

$$\boldsymbol{\sigma}^a=\begin{bmatrix}\sigma & 0\\ 0 & -\lambda^{\mathrm{loc}}\end{bmatrix}\quad\text{and}\quad\boldsymbol{\sigma}^b=\begin{bmatrix}\sigma & 0\\ 0 & 0\end{bmatrix}\tag{18}$$

where σ is a free variable. In addition, the admissibility of the stresses $\boldsymbol{\sigma}^a$ and $\boldsymbol{\sigma}^b$, for the Von Mises yield surface with yield stress σ_Y, gives rise, after taking into account Equations (18), to the following conditions:

$$\begin{aligned}(\sigma+\lambda^{\mathrm{loc}})^2&\leqslant\tfrac{4}{3}\sigma_Y^2\\\sigma^2&\leqslant\tfrac{4}{3}\sigma_Y^2\end{aligned}$$

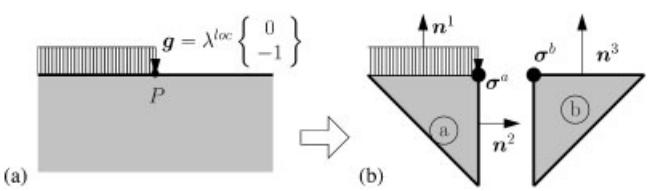

Figure 3. (a) Continuum problem and (b) simplified model with two elements used for the analysis of the lower bound problem.

DOI: 10.1002/nme

The maximum value of λ that satisfies these conditions is given by $\lambda^{\text{loc}}=4\sigma_Y/\sqrt{3}$, which is obtained for $\sigma=-2\sigma_Y/\sqrt{3}$. Three main conclusions can be derived from this result:

1. A maximum value for λ^{loc} has been found. The lower bound problem searches the maximum value of $\lambda=\lambda^{\text{LB}}$ that satisfies all the discretized equilibrium equations in the whole domain. Therefore, in a mesh that contains the local simplified system given above, the values found provide a limitation in the maximum value, i.e. $\lambda^{\text{LB}}\leqslant\lambda^{\text{loc}}$.
2. Any remeshing strategy of the two elements that subdivides each element into four similar elements (see the pattern in Figure 7(a) in the next section) leads to an identical problem as the one considered here and thus leaves the value of λ^{loc} unchanged.
3. If we add one additional element around point P, let us say element c, we are adding three more variables $\boldsymbol{\sigma}^c$ and two more equilibrium equations at the internal edge, plus one more yield condition for $\boldsymbol{\sigma}^c$. Therefore, if the new conditions are independent of the previous ones, the limitation found for the local problem always exists, independently of the number of elements.

In order to verify numerically the last remark, and to test the dependency of λ^{loc} on the geometry of the model, we have modelled the simplified model for different opening angles α of the two free surfaces and for different numbers of elements *nele* (see Figure 4). We have used equilibrium equations at point P equivalent to those written in (17) for each element–element boundary and external edge. This is tantamount to the conditions that the lower bound problem would impose at node P.

In an attempt to capture the slip line exactly for the case $\alpha=180°$, we have performed an additional analysis by adding elements only within a central angle β. The evolution of the λ^{loc} is plotted in Figure 5. Two further conclusions can be extracted:

4. In agreement with point 3 above, a maximum value λ^{loc} is always found.
5. It has been verified in Figure 5 and Table I, that for values of $\beta>90°$ the load factor λ^{loc} converges to the exact solution $(2+\pi)c=5.1415926$, and for $\beta\leqslant 80$, the error decreases much slower or is constant after a certain number of elements.

We found the last point relevant in two aspects. First, there is no need to remesh radially in all directions, and thus it appears reasonable to design a strategy that concentrates elements in those directions that constrain the maximization problem. Second, the load factor of the flexible strip

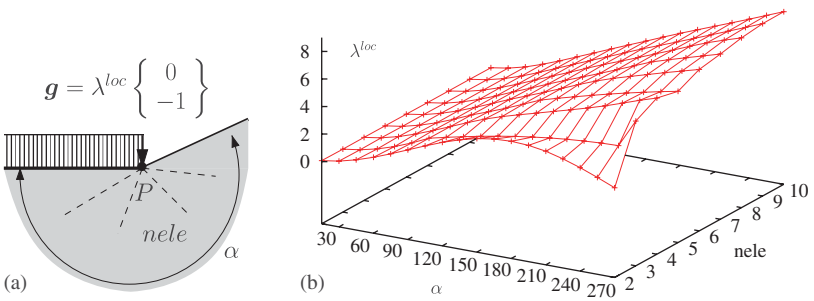

Figure 4. Values of λ^{loc} as a function of α and *nele*.

DOI: 10.1002/nme

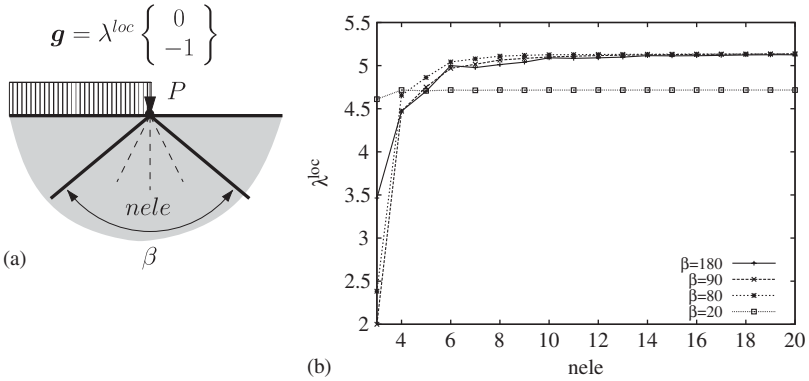

Figure 5. Values of λ^{loc} for $\alpha = 180°$ and different number of elements within different centred angles β.

Table I. Error in percent of λ^{loc} for $\beta = 90$ and 80°.

nele	20	50	100	200	300	400	500	1000
$\lambda^{\text{loc}}(\beta = 90)$	6.527	0.718	0.154	0.035	0.015	0.008	0.005	0.001
$\lambda^{\text{loc}}(\beta = 80)$	6.435	3.907	3.624	3.559	3.547	3.544	3.542	3.539

footing has been found by only studying the solution of a local constrained problem. This means that if the velocity and stress field at the limit load are not desired, an estimate of the load factor may be computed by just analysing the reduced model, which is computational much cheaper than modelling the whole domain. Furthermore, from the tightness of λ^{loc}, we can conclude that this estimate converges to the theoretical load factor and that the latter, in the non-discretized studied problem, is determined by a local phenomenon, independently of the slip lines (or velocity and stress fields).

We have performed the same analysis for a Mohr–Coulomb material, where the locking effect of the lower bound has also been encountered. In this case, the same conclusions have been found. However, instead of the value $N_s = (2+\pi)c$, the solution converged towards the Prandt solution, which is given by [1, 26]

$$\lambda = c(\mathrm{e}^{\pi \tan \phi} \tan^2(45 + \phi/2) - 1) \cot \phi$$

In particular, for the values $c = 1$ and $\phi = 30°$, this expression yields $\lambda = 30.13962$, which is the limit value of the local problem (see Figure 6).

It can then be concluded that the radial subdivision of the affected elements (see the pattern in Figure 7(b)) appears as a reasonable strategy. Further analyses using more general optimal angular distributions of elements are necessary, and research along this line is currently being carried out. Also, the conditions for the existence of a local problem in a general limit analysis and whether the observed behaviour for the strip footing can be extended in three-dimensional for a footing slab must still be investigated.

DOI: 10.1002/nme

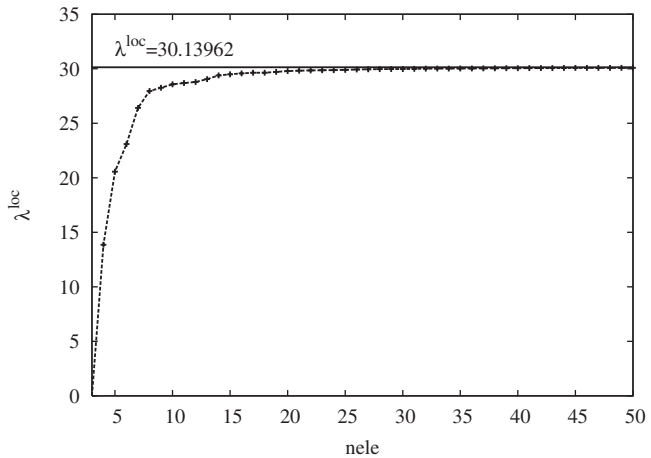

Figure 6. Evolution of λ^{loc} as a function of the number of elements for a Mohr–Coulomb material with $c=1$ and $\phi=30°$.

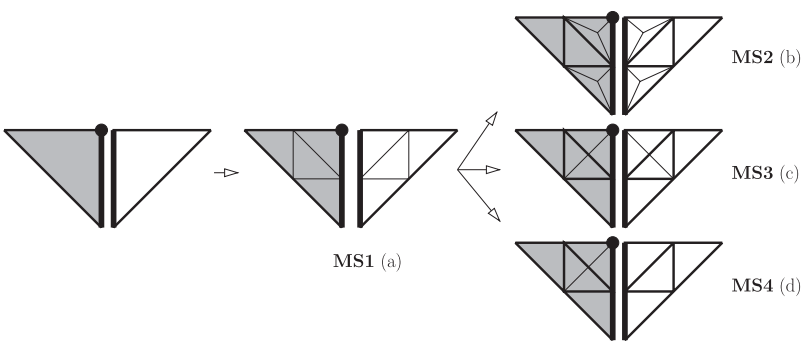

Figure 7. Patterns used in remeshing strategies MS1–MS4. Selected element, edge and node are indicated with light grey, thick line and large bold dot, respectively.

6. MESH ADAPTIVITY

In order to capture the localization of the strains and stresses that characterize the solution of limit analysis, the design of an efficient mesh adaptivity strategy is highly desirable. In Section 6.1 we introduce two error estimates, one associated with the elements and another associated with the internal edges. The latter permits one to construct fan-type meshes, which are necessary to overcome the locking phenomenon when discontinuous surface loading exists. In addition, from the conclusions in the previous section, two meshing strategies are described in Section 6.2, which additionally take into account either the edge velocities of the lower bound problem or the velocity jumps of the upper bound problem. Alternatively, when no fan-type patterns are required, we also introduce a meshing strategy that provides a non-embedded mesh.

DOI: 10.1002/nme

6.1. Elemental error estimate

It is shown in Appendix D that the global bound gap $\lambda^{\mathrm{UB}}-\lambda^{\mathrm{LB}}$ may be expressed as the sum of elemental contributions Δ_λ^e plus the sum of contributions Δ_λ^ξ arising from the discontinuity of the velocity field across the internal edges, i.e.

$$\lambda^{\mathrm{UB}}-\lambda^{\mathrm{LB}}=\sum_{e=1}^{nele}\Delta_\lambda^e+\sum_{\xi=1}^{N_I}\Delta_\lambda^\xi$$

The elemental and edge contributions are, respectively, given by

$$\Delta_\lambda^e=D^e(\mathbf{u}^{\mathrm{UB}})-\underbrace{\left(\int_{\Omega^e}(-\nabla\cdot\boldsymbol{\sigma}^{\mathrm{LB}})\cdot\mathbf{u}^{\mathrm{UB}}\,\mathrm{d}V+\int_{\partial\Omega^e}(\mathbf{n}^e\cdot\boldsymbol{\sigma}^{\mathrm{LB}})\cdot\mathbf{u}^{\mathrm{UB}}\,\mathrm{d}\Gamma\right)}_{l^e(\mathbf{u}^{\mathrm{UB}})} \tag{19a}$$

$$\Delta_\lambda^\xi=D^\xi(\mathbf{u}^{\mathrm{UB}})+\int_{\xi^{e-e'}}\boldsymbol{\sigma}^{\mathrm{LB}}\mathbf{n}\cdot[\![\mathbf{u}^{\mathrm{UB}}]\!]\,\mathrm{d}\Gamma \tag{19b}$$

where the expression of the elemental plastic dissipation rates $D^e(\mathbf{u}^{\mathrm{UB}})$ and $D^\xi(\mathbf{u}^{\mathrm{UB}})$ depends on the plasticity criteria. For Von Mises they are given by

$$D^e(\mathbf{u}^{\mathrm{UB}})=\int_{\Omega^e}\sigma_Y\varepsilon_{\mathrm{eq}}\,\mathrm{d}V$$

$$D^\xi(\mathbf{u}^{\mathrm{UB}})=\int_{\xi^{e-e'}}\frac{\sigma_Y}{\sqrt{3}}|[\![\mathbf{u}^{\mathrm{UB}}]\!]|\,\mathrm{d}\Gamma$$

whereas for Mohr–Coulomb they are expressed as

$$D^e(\mathbf{u}^{\mathrm{UB}})=\int_{\Omega^e}c\sqrt{\frac{3}{1+2\tan^2\phi}}\varepsilon_{\mathrm{eq}}\,\mathrm{d}V$$

$$D^\xi(\mathbf{u}^{\mathrm{UB}})=\int_{\xi^{e-e'}}c\cos\phi|[\![\mathbf{u}^{\mathrm{UB}}]\!]|\,\mathrm{d}\Gamma$$

We note that the elemental gap Δ_λ^e is the same employed in [9, 10], where it is demonstrated that $\Delta_\lambda^e\geqslant 0$. Furthermore, since by definition

$$D^\xi(\mathbf{u}^{\mathrm{UB}})=\max_{\mathbf{t}^{\mathrm{UB}}\in\mathscr{B}_t^{\mathrm{UB}}}\int_{\xi^{e-e'}}\mathbf{t}^{\mathrm{UB}}\cdot[\![\mathbf{u}^{\mathrm{UB}}]\!]\,\mathrm{d}\Gamma$$

and we have imposed the membership conditions $\mathscr{B}^{\mathrm{UB}}\supseteq\mathscr{B}$ and $\boldsymbol{\sigma}^{\mathrm{LB}}\in\mathscr{B}$, we have that $D^\xi(\mathbf{u})\geqslant\int_{\xi^{e-e'}}\boldsymbol{\sigma}^{\mathrm{LB}}\mathbf{n}\cdot[\![\mathbf{u}^{\mathrm{UB}}]\!]\,\mathrm{d}\Gamma$, and therefore $\Delta_\lambda^\xi\geqslant 0$. The two contributions Δ_λ^e and Δ_λ^ξ are positive and thus valid candidates for error estimates.

Consequently, the elements and edges that must be remeshed may be chosen according to their contribution to the bound gap. After computing the maximum element or edge bound gap

DOI: 10.1002/nme

$\Delta_{\max} = \max_{e,\xi} \Delta_{\lambda}^{e,\xi}$, we will remesh those entities for which

$$\Delta_{\lambda}^{e} > \eta_{\Delta} \Delta_{\max} \tag{20a}$$

$$\Delta_{\lambda}^{\xi} > \eta_{\Delta} \Delta_{\max} \tag{20b}$$

where η_{Δ} is a chosen threshold for the bound gap, with $0 \leqslant \eta_{\Delta} \leqslant 1$. The subdivision of each element is performed according to the following two remeshing strategies:

*MS*1: If the error contribution of an element interior satisfies (20a), or any of its edges satisfy (20b), the element will be quadrisected according to the pattern in Figure 7(a). Other elements may be additionally remeshed in order to build a conforming mesh.

*MS*2: In addition to remeshing strategy MS1, the elements that have edges satisfying condition (20b) are subdivided according to the pattern in Figure 7(b).

It will be shown in the numerical examples that when the remeshing strategy MS1 is not able to overcome the locking of the lower bound, strategy MS2 introduces the necessary radial elements to prevent it. We note that the latter may worsen the aspect ratio of some elements in internal areas where no discontinuous loading is applied. For this reason, two additional remeshing strategies have been designed, which will be described in the next paragraphs.

6.2. Radial remeshing strategies

It has been verified numerically that in problems with discontinuous Neumann conditions, such as the strip footing problem analysed in Section 7.1 or the model analysed in Section 5, the only active constraints are those at the edges of the elements connected to the point where the load is discontinuous. Since the edge velocities are conjugated to the edge equilibrium equations, the following remeshing strategies are proposed:

*MS*3: We define, for each node a, the following resultant of the edge velocities:

$$\Delta \mathbf{u}_{\xi}^{a} = \sum_{e \ni a} \mathbf{u}_{\xi_1}^{a,e} - \mathbf{u}_{\xi_2}^{a,e}$$

where $\mathbf{u}_{\xi_1}^{a,e}$ and $\mathbf{u}_{\xi_2}^{a,e}$ are the edge velocities of the lower bound problem, for those edges belonging to element e, which is connected to node a. By definition, $\Delta \mathbf{u}_{\xi}^{a} = \mathbf{0}$ at the internal nodes and therefore is a suitable candidate to detect those equilibrium equations at the edges that constrain exceedingly or even block the lower bound solution. After applying remeshing strategy MS1, strategy MS3 applies the remeshing pattern shown in Figure 7(c) (fan-type subdivision in all directions around a selected node) to those nodes that satisfy $\|\Delta \mathbf{u}_{\xi}^{a}\| \leqslant \eta_u \max_a \|\Delta \mathbf{u}_{\xi}^{a}\|$, where η_u is a threshold parameter, with $0 \leqslant \eta_u \leqslant 1$.

*MS*4: It has been numerically tested that the slip lines in a limit analysis problem are better represented by the discontinuities of the piecewise linear velocity field of the upper bound problem. For this reason, we define the following jump of the tangent edge velocities for each node a of each element e:

$$\bar{\mathbf{u}}_{\tau}^{a,e} = \mathbf{u}_{\tau\xi_1}^{a,e} + \mathbf{u}_{\tau\xi_2}^{a,e}$$

where $\mathbf{u}_{\tau\xi i}^{a,e} = (\mathbf{I} - \mathbf{n}_{\xi_i} \otimes \mathbf{n}_{\xi_i}) [\![\mathbf{u}^{a,e}]\!]$ is the jump of the upper bound tangent velocity across the edge $\xi_i, i = 1, 2$ of element e at node a. Strategy MS4 remeshes radially those nodes where $\|\bar{\mathbf{u}}_{\tau}^{a,e}\| \leqslant \eta_u \max_{a,e} \|\bar{\mathbf{u}}_{\tau}^{a,e}\|$, with η_u a threshold parameter. These nodes are radially remeshed according to the pattern in Figure 7(d), i.e. only in the direction where element e is located.

DOI: 10.1002/nme

6.3. Non-embedded remeshing strategy

In many practical problems, the tightness of the load factor bounds is strongly dependent on the mesh orientation, which, when using embedded remeshing strategies, is in turn given by the initial mesh. In order to avoid this dependence, we have also implemented a non-embedded adaptive strategy, which we note has the advantage of allowing mesh de-refinement.

The new elemental mesh size $\hat{h}^e$ is obtained by applying a standard Richardson extrapolation to the linear elements employed here. Accordingly, assuming that the solution is mostly regular, the desired nodal mesh size may be computed from the elemental error estimates in (19a) as follows [27]:

$$\hat{h^e} = h^e \sqrt{\frac{\hat{\Delta}^e_\lambda}{\Delta^e_\lambda}} \tag{21}$$

where $\hat{\Delta}^e_\lambda = \eta_\Delta \max_e \Delta^e_\lambda$ is the desired maximum elemental gap at the next iteration. Owing to the presence of very small elemental gaps in areas that behave as rigid blocks, the resulting mesh size $\hat{h^e}$ may become too large or yield ill-posed mesh size fields (the variations of the mesh size are too sharp). For these reasons, in Equation (21), instead of the elemental gap Δ^e_λ, we have employed the larger value:

$$\tilde{\Delta}^e_\lambda = \sqrt{(\bar{\Delta}^e_\lambda)^2 + (\Delta^e_\lambda)^2} \tag{22}$$

where $\bar{\Delta}^e_\lambda = \sum_{n \in e} \Delta^n_\lambda / 3$ is an averaged elemental gaps computed from the set of nodal gaps Δ^n_λ. The latter are the maximum elemental gap of the N^e_n elements connected to node n, i.e. $\Delta^n_\lambda = \max_{e \ni n} \Delta^e_\lambda$.

Standard remeshing algorithms make use of a pointwise field with the desired new mesh size. In the present case, we have used the EZ4U package [28], which requires the nodal values of the new mesh size. This nodal mesh size is extracted from the elemental mesh sizes $\hat{h}^e$ in (21) by weighting the elemental values with the elemental areas A_e:

$$\bar{h}_n = \frac{\sum_{e \ni n} \hat{h}_e \sqrt{A_e}}{\sum_{e \ni n} \sqrt{A_e}} \tag{23}$$

With this notation at hand, the non-embedding remeshing strategy may be stated as follows:

*MS*5: Define new elemental mesh sizes by using $\hat{h}^e = h^e \sqrt{\hat{\Delta}^e_\lambda / \bar{\Delta}^e_\lambda}$, with $\bar{\Delta}^e_\lambda$ in (22), and from these values, compute the nodal mesh sizes in Equation (23).

7. NUMERICAL EXAMPLES

7.1. Flexible strip footing

This problem has been widely studied elsewhere [7, 8, 11, 12, 17, 18, 23, 29], but it is analysed here to show that the mesh strategies MS2–MS4 converge to the theoretical load factor satisfactorily due to the introduction of a fan-type mesh around the point with the surface load discontinuity. The load of a flexible strip footing is applied on an assumed weightless soil (see Figure 8(a)). For a purely cohesive material ($\phi = 0°$) in plane strain, the analytical solution is given by $\lambda/c = (2+\pi)c$ [1].

DOI: 10.1002/nme

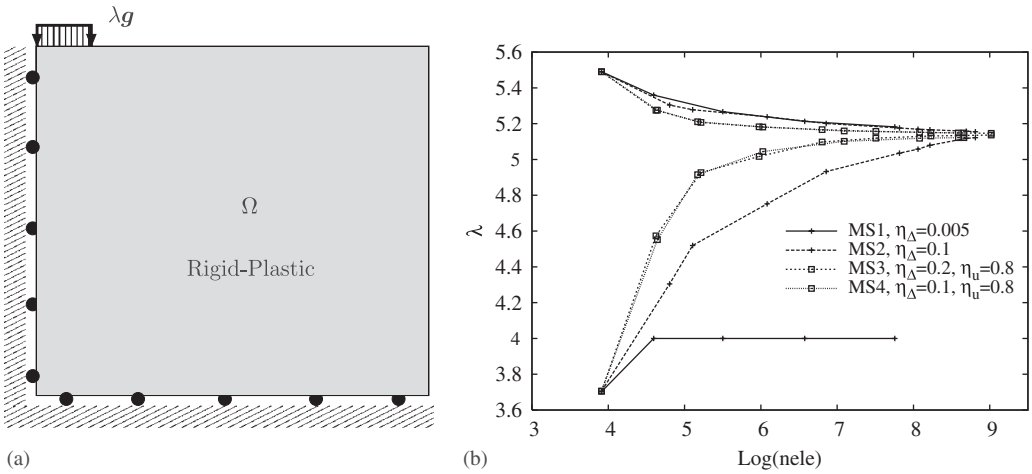

Figure 8. Strip footing. Geometry (a) and evolution of bounds using strategies MS1–MS4 (b).

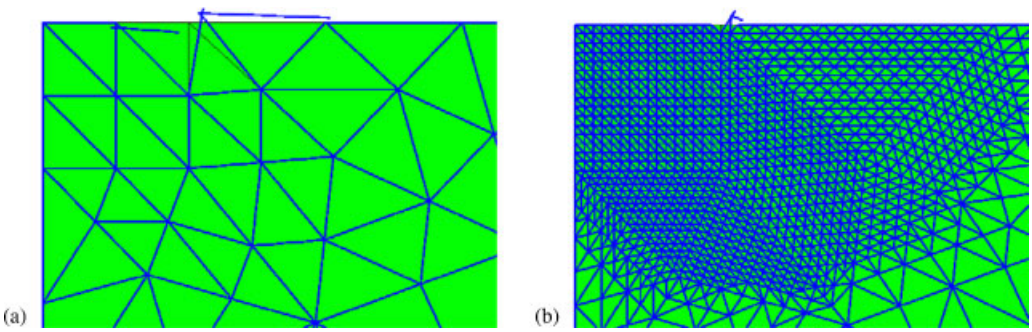

Figure 9. Strip footing problem. Edge velocities (line elements) and body velocities (equal to zero) with a (a) coarse mesh and (b) a finer mesh.

In order to illustrate the effect of the remeshing strategy, we have plotted in Figure 9 the linear velocities of the edges and the constant velocities of the body element. We recall that these are conjugate to the body equilibrium equations, $\nabla\cdot\boldsymbol{\sigma}+\lambda\mathbf{f}=\mathbf{0}$, and the edge equilibrium equations, $(\boldsymbol{\sigma}^{e}-\boldsymbol{\sigma}^{e'})\cdot\mathbf{n}^{e-e'}=\mathbf{0}$. It emerges from the graphs that the only active constraints are the latter edge equilibrium relations (the body velocities are practically zero).

As it can be observed from the evolutions of the bounds in Figure 8(b), meshing strategies MS2–MS4 prevent the locking of the lower bound. Figure 10 shows the resulting meshes after employing nine, seven and six iterations, respectively. From the comparison of the four strategies in Figures 8(b) and 10 it can be concluded that strategy MS2 has a worse convergence than MS3 and MS4. This is due to the fact that the contributions of the edges to the bound gap are not solely due to the presence of the discontinuous load, as the distributed remeshed areas in Figure 10(a) show. We also point out that although the meshes of strategies MS3 and MS4 are more concentrated

DOI: 10.1002/nme

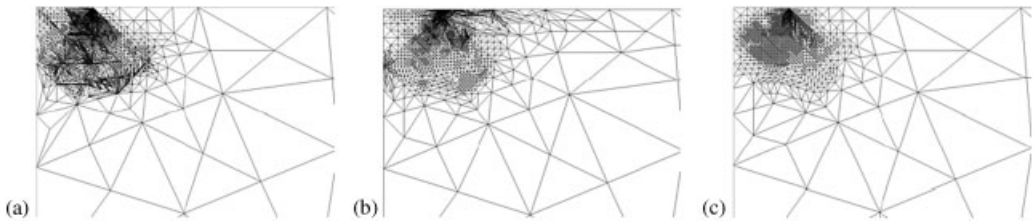

Figure 10. Strip footing problem: detail of the mesh in the upper left corner showing the point with surface load discontinuity. Mesh using strategies MS2 (after nine iterations with $\eta_\Delta = 0.1$) (a), MS3 (after seven iterations with $\eta_u = 0.2$ and $\eta_u = 0.8$) (b), and MS4 (after six iterations with $\eta_u = 0.1$ and $\eta_u = 0.8$) (c).

at the point with the load discontinuity, they still contain some extended areas that are finely meshed. This drawback may be caused by the impossibility to reproduce rigidly rotated areas with the piecewise constant velocity field of the lower bound problem. It is interesting to remark that the limit load factor for this problem can be estimated by just analysing the point with the load discontinuity, which in fact requires a minimal number of elements (see the analysis in Section 5). Indeed, the local analysis with 12 elements leads to a load factor estimate (5.1165) that is better than the analysis of the whole domain with more than 3000 elements (5.1148).

7.2. Vertical cut

Figure 11 depicts the geometry and boundary conditions of this problem, which has been also analysed in [7, 17, 23] discretized with uniform meshes, and in [18, 22] using adaptive remeshing. The stability of the vertical cut in a purely cohesive soil ($\phi = 0$) is given by the parameter $N_s = H\gamma/c$, where γ is the soil density and c is the cohesion. The tighter computed lower bound for N_s has been reported in [7]. In [18], an anisotropic error estimate is used, which requires an optimal-mesh adaptive scheme that solves an optimization problem for the computation of the new element sizes. Our error estimate requires just to evaluate expression (19a) and apparently can slightly improve the lower bound given in [18] for a similar number of elements. Table II compares the bounds obtained with the analysis in the literature and the present work with the initial mesh in Figure 11(b). A further run with 15 214 elements yields the values $N^{\mathrm{LB}} = 3.7748$ and $N^{\mathrm{UB}} = 3.7849$. As a reference, the latter analysis took 237 and 438 s for the lower and upper bound problems, respectively, when using a PC with 3 GHz and 1 GB of RAM and solving the SOCP with SDPT3-4.0.

In order to test the mesh dependence of the results, we have also run the test with MS1 and using the initial mesh in Figure 11(c) (the internal edges of the two elements at the top left corner do not follow the 45° slip line). In this case, the lower bound was reduced to $N_s = 3.76815$ when using 12 518 elements. This fact suggests that the evolution of the upper and lower bounds depend on the initial mesh when using an embedded remeshing strategy. We have also used strategy MS5, which improved the latter result, although it could not improve the lower bounds of MS1 applied to the mesh in Figure 11(b). Table III contains the lower bounds obtained for the three tests, and Figures 12(a) and (b) show the final meshes when using strategies MS1 and MS5. Figures 12(c) and (d) show a contour plot of the internal dissipation energy rate. Interestingly, it can be observed that despite the two meshes reproduce more than one slip line, the dissipative energy is concentrated

DOI: 10.1002/nme

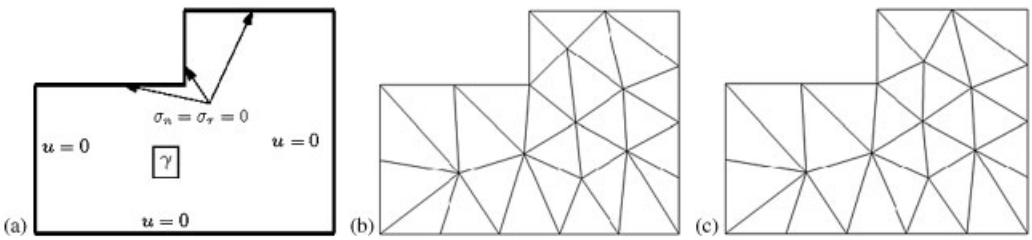

Figure 11. Vertical cut problem. (a) Geometry and two initial meshes considered (b) and (c).

Table II. Vertical cut problem. Comparison of bounds obtained by Lyamin and Sloan [7, 18] and in the present work, using strategy MS1.

	Lower bound		Upper bound	
Reference	# elements	N_s	# elements	N_s
Lyamin *et al.* [7, 17]	2880	3.763	1110	3.801
	6400	3.772	2928	3.794
Lyamin *et al.* [18]	500	3.71	—	—
	2000	3.76	—	—
Present work	595	3.7352	595	3.8712
(MS1 with the initial	1864	3.7643	1864	3.8223
mesh in Figure 11(b))	6926	3.7728	6926	3.7962

Table III. Vertical cut problem. Comparison of lower bounds obtained using strategy MS1 with initial mesh in Figure 11b, strategy MS1 with initial mesh in Figure 11(c), and strategy MS5.

MS1, mesh Figure 11(b)			MS1, mesh Figure 11(c)			MS5		
# elem.	LB	UB	# elem.	LB	UB	# elem.	LB	UB
595	3.7352	3.8712	546	3.6877	3.8906	578	3.6253	3.9533
14 887	3.7743	3.7877	10 742	3.7704	3.7969	12 180	3.7731	3.8127

along one single area located within the apparent slip lines. This discrepancy between the values of the error estimate and the areas with higher dissipated energy may be due to two reasons: either the remeshing strategy shall be improved in order to concentrate finely meshed areas in a single slip line or the actual collapse mechanism contains a slip band with a non-negligible thickness. Although our results are prone to the latter situation, the computation of tighter bound gaps is still necessary to verify this conclusion.

7.3. Squared plate with asymmetric holes

This problem has been originally modelled in [30] in the context of viscoplasticity and in compression, and by Zouain *et al.* [24] using a mixed element for shakedown analysis. Makrodimopoulos

DOI: 10.1002/nme

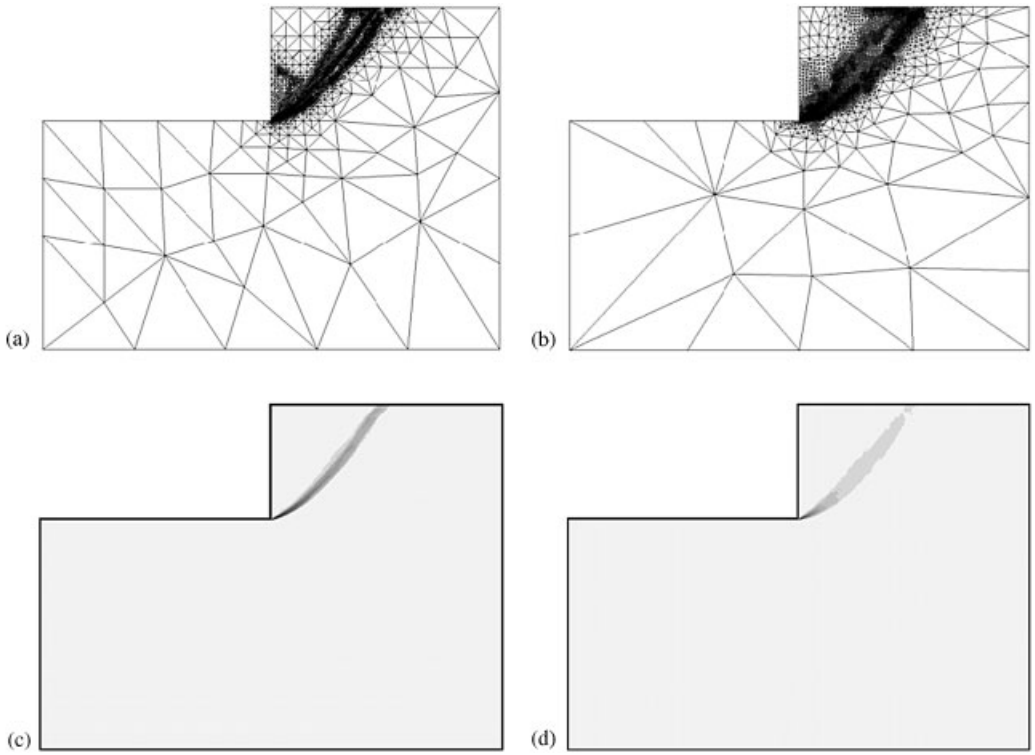

Figure 12. Vertical cut problem: final mesh using strategy MS1, 14 887 elements (a) and strategy MS5, 9346 elements (b). The contour plots of the internal dissipation rate for meshes (a) and (b) are shown in (c) and (d), respectively.

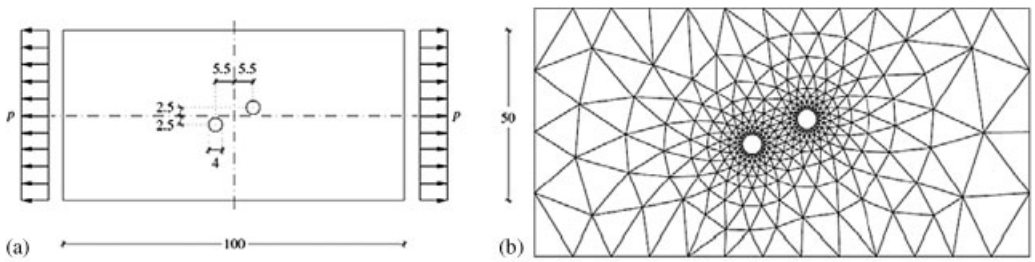

Figure 13. (a) Geometry and (b) initial mesh employed in the problem of two asymmetric holes.

and Martin [8] have used the same lower bound interpolation described here, together with the SOCP package MOSEK [16]. However, they have not applied any adaptive remeshing strategy. Thus, we manage to obtain tighter bounds for a similar number of elements (see Table IV) using the initial mesh in Figure 13. Moreover, the resulting meshes when using strategy MS1 (see Figure 14)

DOI: 10.1002/nme

Table IV. Comparison of lower bounds obtained in [8] and in the present work using strategy MS1.

	$\phi=0°$			$\phi=30°$		
		p/c			p/c	
Reference	# elements	LB	UB	# elements	LB	UB
Makrodimopoulos and Martin [8]	2996	1.7840	—	2996	1.0464	—
	12 738	1.8089	—	12 738	1.0562	—
Present work	1744	1.8018	1.8601	1178	1.0565	1.0820
	13 699	1.8119	1.8351	12 710	1.0581	1.0652

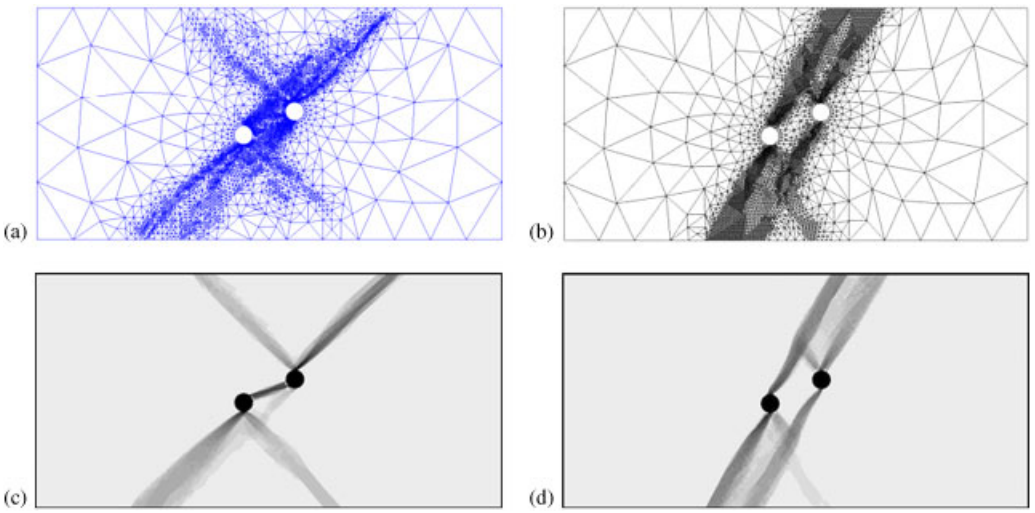

Figure 14. Final mesh with 10 778 elements employed in the problem of two asymmetric holes with (a) $\phi=0°$ and (b) $\phi=30°$.

in a purely cohesive material (Tresca criteria, $c=1$, $\phi=0°$) and a cohesive-frictional ($\phi=30°$) material reveal the different failure mechanisms obtained in each case.

8. CONCLUSIONS

The upper and lower bound problems of limit analysis have been written as second-order optimization problems. By using adequate interpolation spaces for the stress and velocity fields [9–12], the solution of each optimization problem furnishes strict bounds of the load factor, and a set of discretized stress and velocity fields.

We have extended the formulation in [9, 10], written for Von Mises criterion, by adapting the structure of the problem to two-dimensional Mohr–Coulomb plasticity. In both cases, the membership constraints may be written as quadratic constraints, which gives rise to an optimization

DOI: 10.1002/nme

problem that is suited for Second-Order Conic Programming (SOCP), and can be solved resorting to recently developed packages [14, 15].

The stress and velocity fields of the upper and lower bound problem are used to construct an *a posteriori* error estimate, which includes contributions from the elements and from the interior edges. From these error estimates, we have presented remeshing strategy MS1, which can furnish, for the examples shown here and using similar number of elements, better bounds than those given in existing references.

Special regard has been paid to the analysis of problems with discontinuous surface loading. Although the need of fan-type mesh patterns is well recognized in the literature, we have highlighted the sources of the locking phenomenon in the absence of these mesh patterns, and studied a local problem that includes the point where the surface load is discontinuous. From this analysis and the numerical results, and resorting to the edge contributions or the discontinuities of the velocity field, we have designed remeshing strategies MS2–MS4 that add elements in a fan-type pattern and that are able to radially mesh only in the necessary directions. In this manner, the locking of the lower bound has been prevented. Furthermore, it has been observed that the value of the load factor of the whole domain can be estimated by analysing this local problem, which has far less elements than the global problem. Although the local problem studied here is characterized by a discontinuous external load, the general determination and classification of such local problems in limit analysis is still an open question.

APPENDIX A: SPECIFIC EXPRESSIONS FOR VON MISES AND MOHR–COULOMB PLASTICITY

In Von Mises plasticity, the yield function is given by

$$f(\boldsymbol{\sigma}) = \sqrt{\operatorname{dev}\boldsymbol{\sigma} : \operatorname{dev}\boldsymbol{\sigma}} - \sqrt{\tfrac{2}{3}}\sigma_Y \tag{A1}$$

where σ_Y is the yield stress and $\operatorname{dev}\boldsymbol{\sigma}$ is the deviatoric part of $\boldsymbol{\sigma}$. From the associative rule $\varepsilon = \gamma \partial f(\boldsymbol{\sigma})/\boldsymbol{\sigma} = \gamma \operatorname{dev}\boldsymbol{\sigma}/\sqrt{\operatorname{dev}\boldsymbol{\sigma} : \operatorname{dev}\boldsymbol{\sigma}}$, and the definition of the internal work dissipation (5), it follows that $D(\mathbf{u})$ and $\varepsilon_{\mathrm{eq}}(\mathbf{u})$ can be expressed as

$$D(\mathbf{u})_{\mathrm{VM}} = \int_\Omega \sigma_Y \varepsilon_{\mathrm{eq}} \, \mathrm{d}V$$

where $\varepsilon_{\mathrm{eq}}(\mathbf{u}) = \sqrt{(2/3)\varepsilon(\mathbf{u}) : \varepsilon(\mathbf{u})}$ is the equivalent strain. In two-dimensional plane strain analysis, the yield function in (A1) is expressed as

$$f(\boldsymbol{\sigma}) = \sqrt{(\sigma_{xx} - \sigma_{yy})^2 + 4\sigma_{xy}^2} - \frac{2}{\sqrt{3}}\sigma_Y$$

By applying the following transformation of the stress variables $\boldsymbol{\sigma}^{\mathrm{T}} = \{\sigma_{xx} \ \sigma_{yy} \ \sigma_{xy}\}$:

$$\mathbf{x}_{24} = \begin{Bmatrix} x_2 \\ x_3 \\ x_4 \end{Bmatrix} = \mathbf{M}_{\mathrm{VM}}^{-1}\boldsymbol{\sigma}, \quad \mathbf{M}_{\mathrm{VM}}^{-1} = \begin{bmatrix} 0 & 0 & 2 \\ 1 & -1 & 0 \\ 1 & 0 & 0 \end{bmatrix} \tag{A2}$$

DOI: 10.1002/nme

the membership constraint $\boldsymbol{\sigma} \in \mathscr{B} = \{\boldsymbol{\sigma} \,|\, f(\boldsymbol{\sigma}) \leqslant 0\}$ is equivalent to the following set of constraints:

$$\mathbf{x}_{13} \in \mathscr{L}^3, \quad x_1 = \frac{2}{\sqrt{3}}\sigma_Y, \quad x_4 \text{ free} \tag{A3}$$

where $\mathscr{L}^3 = \{\mathbf{x} \in \mathbb{R}^3 | x_1 \geqslant \sqrt{x_2^2 + x_3^2}\}$ is the three-dimensional Lorentz cone.

Regarding Mohr–Coulomb plasticity, its yield function for two-dimensional analysis reads

$$f(\boldsymbol{\sigma}) = \sqrt{(\sigma_{xx} - \sigma_{yy})^2 + 4\sigma_{xy}^2} + (\sigma_{xx} + \sigma_{yy}) \sin\phi - 2c\cos\phi$$

where c and ϕ are the soil cohesion and internal friction angle. The rate of plastic dissipation is accordingly given by

$$D(\mathbf{u})_{\mathrm{MC}} = \int_\Omega c \sqrt{\frac{3}{1 + 2\tan^2\phi}} \varepsilon_{\mathrm{eq}} \, \mathrm{d}V$$

By transforming the stress variables as

$$\mathbf{x}_{13} = \begin{Bmatrix} x_1 \\ x_2 \\ x_3 \end{Bmatrix} = \mathbf{M}_{\mathrm{MC}}^{-1}\boldsymbol{\sigma} + \mathbf{d} \tag{A4a}$$

where

$$\mathbf{M}_{\mathrm{MC}}^{-1} = \begin{bmatrix} -\sin\phi & -\sin\phi & 0 \\ 0 & 0 & 2 \\ 1 & -1 & 0 \end{bmatrix}, \quad \mathbf{d} = \begin{Bmatrix} 2c\cos\phi \\ 0 \\ 0 \end{Bmatrix} \tag{A4b}$$

we can replace the condition $\boldsymbol{\sigma} \in \mathscr{B}$ by $\mathbf{x}_{13} \in \mathscr{L}^3$. If $\phi = 0$, the same transformation used for Von Mises plasticity can be used here, but replacing the equality constraint in (A3) $x_1 = \frac{2}{\sqrt{3}}\sigma_Y$ by $x_1 = 2c$.

Note that since matrices $\mathbf{M}_{\mathrm{VM}}^{-1}$ and $\mathbf{M}_{\mathrm{MC}}^{-1}$ in (A2) and (A4b) are invertible, we can express $\boldsymbol{\sigma}$ as a function of the $\mathbf{x}$ variables:

$$\boldsymbol{\sigma} = \mathbf{M}_{\mathrm{VM}}\mathbf{x}_{24}, \quad \boldsymbol{\sigma} = \mathbf{M}_{\mathrm{MC}}\mathbf{x}_{13} - \mathbf{M}_{\mathrm{MC}}\mathbf{d} \tag{A5a}$$

DOI: 10.1002/nme

where

$$\mathbf{M}_{\mathrm{VM}}=\begin{bmatrix} 0 & 0 & 1 \\ 0 & -1 & 1 \\ 0.5 & 0 & 0 \end{bmatrix}, \quad \mathbf{M}_{\mathrm{MC}}=\frac{1}{2}\begin{bmatrix} (\sin\phi)^{-1} & 0 & 1 \\ (\sin\phi)^{-1} & 0 & -1 \\ 0 & 1 & 0 \end{bmatrix} \tag{A5b}$$

APPENDIX B: DISCRETE LOWER BOUND PROBLEM

We next write the algebraic form of the discrete lower bound problem in (11). Full details of the implementation can be found in [9, 10, 12], and we will give here the mean steps towards the construction of the final optimization problem.

For each element e, we denote the elemental stress vector by $\boldsymbol{\sigma}^{e\,\mathrm{T}}=\{\boldsymbol{\sigma}^{e,1\,\mathrm{T}}\ \boldsymbol{\sigma}^{e,2\,\mathrm{T}}\ \boldsymbol{\sigma}^{e,3\,\mathrm{T}}\}$, with $\boldsymbol{\sigma}^{e,n\,\mathrm{T}}=\{\sigma_{xx}^{e,n}\ \sigma_{yy}^{e,n}\ \sigma_{xy}^{e,n}\}$, $n=1,2,3$, the nodal stresses. On the other hand, we note that since the stresses are linear, imposing the second and third equality constraints at the whole edge is equivalent to imposing them at each node of the edge. Consequently, the first two equality constraints in (11) may be then expressed as

$$\mathbf{A}^e\boldsymbol{\sigma}^e+\lambda\mathbf{f}^e=\mathbf{0}, \quad e=1,\ldots,nele \tag{B1a}$$

$$\mathbf{N}^n\boldsymbol{\sigma}^{n,e}+\lambda\mathbf{g}^{n,e}=\mathbf{0}, \quad e,n\in\xi^g \tag{B1b}$$

where ξ^g is the set of external boundaries with Neumann conditions, and condition (B1a) is imposed at the nodes connected to those edges, with normal vector $\mathbf{n}_{\xi^g}^{\mathrm{T}}=\{n_x\ n_y\}$. Matrices $\mathbf{A}^e$ and $\mathbf{N}^e$ are given by

$$\mathbf{A}^e=[\mathbf{D}^1\ \mathbf{D}^2\ \mathbf{D}^3], \quad \mathbf{D}^n=\begin{bmatrix} I_{,x}^n & 0 & I_{,y}^n \\ 0 & I_{,y}^n & I_{,x}^n \end{bmatrix} \tag{B2a}$$

$$\mathbf{N}^n=\begin{bmatrix} n_x & 0 & n_y \\ 0 & n_y & n_x \end{bmatrix} \tag{B2b}$$

where $I_{,x}^n$ and $I_{,y}^n$ are the derivatives of the interpolating functions of node n with respect to x and y, respectively. Note that, in order to ensure exact equilibrium, we have to assume that the body loads $\mathbf{f}$ and the surface loads $\mathbf{g}$ are, at most, constant at each element and linear at each edge, respectively. Their elemental and nodal values are given in the vectors $\mathbf{f}^e$ and $\mathbf{g}^{n,e}$ in (B1). The third equality constraint in (11) is the equilibrium equation at the internal edges. Any pair of elements e and e', with a common edge $\xi^{e-e'}$ and with a normal vector $\mathbf{n}^{e-e'}$, leads to two nodal equations that are expressed as

$$\mathbf{N}^n\boldsymbol{\sigma}^{n,e}-\mathbf{N}^n\boldsymbol{\sigma}^{n,e'}=\mathbf{0}, \quad e,e',n\in\xi^{e-e'} \tag{B3}$$

DOI: 10.1002/nme

where $\mathbf{N}^n$ has the same form as in (B2b). The assembling of the elemental (B1) and (B3), together with the membership constraint in (11), leads to the following global optimization problem:

$$\begin{aligned} \max \quad & \lambda \\ \text{s.t.} \quad & \begin{cases} \begin{bmatrix} \mathbf{f} & \mathbf{A} \\ \mathbf{g} & \mathbf{N}^g \\ \mathbf{0} & \mathbf{N}^{e-e'} \end{bmatrix} \begin{Bmatrix} \lambda \\ \boldsymbol{\sigma}^{\mathrm{LB}} \end{Bmatrix} = \mathbf{0} \\ \boldsymbol{\sigma}^{e,n} \in \mathscr{B}, \quad n=1,2,3;\ e=1,\ldots,nele \end{cases} \end{aligned} \tag{B4}$$

Matrix $\mathbf{A}$ and vectors $\mathbf{f}$ and $\mathbf{g}$ are the assembling of the elemental and nodal contributions of $\mathbf{A}^e$, $\mathbf{f}^e$ and $\mathbf{g}^e$, respectively, whereas matrices $\mathbf{N}^g$ and $\mathbf{N}^e_{e'}$ are the assembled nodal matrices $\mathbf{N}^n$ in (B1b) and (B3), respectively. The vector $\boldsymbol{\sigma}^{\mathrm{LB}}$ corresponds to the whole set of nodal stresses and has $3\times3\times nele$ scalar components. In order to write the membership constraint as a second-order conic constraint, a linear transformation of the nodal stresses is required. It is shown in Appendix A that in Von Mises plasticity or in Mohr–Coulomb with $\phi=0$, it is convenient to introduce the variable $\mathbf{x}^{n,e}_{14}=\{x^{n,e}_1\ x^{n,e}_2\ x^{n,e}_3\ x^{n,e}_4\}$ and use the elemental transformation:

$$\boldsymbol{\sigma}^{n,e}=\mathbf{M}_{\mathrm{VM}}\mathbf{x}^{n,e}_{24} \tag{B5}$$

together with the condition $x_1=2\sigma_Y/\sqrt{3}$ or $x_1=2c$. In Mohr–Coulomb plasticity with $\phi\neq0$, we use the variable $\mathbf{x}^{n,e}_{13}=\{x^{n,e}_1 x^{n,e}_2 x^{n,e}_3\}$ and the transformation

$$\boldsymbol{\sigma}^{n,e}=\mathbf{M}_{\mathrm{MC}}\mathbf{x}^{n,e}_{13}-\mathbf{M}_{\mathrm{MC}}\mathbf{d} \tag{B6}$$

Explicit expressions for matrices $\mathbf{M}_{\mathrm{VM}}$ and $\mathbf{M}_{\mathrm{MC}}$ and vector $\mathbf{d}$ are given in Equations (A4b) and (A5) of Appendix A. Inserting the transformation (B5) into the constraints in (B4) yields the following optimization problem:

$$\begin{aligned} \max \quad & \lambda \\ \text{s.t.} \quad & \begin{cases} \begin{bmatrix} \mathbf{f} & \mathbf{0} & \mathbf{A}_M \\ \mathbf{g} & \mathbf{0} & \mathbf{N}^g_M \\ \mathbf{0} & \mathbf{0} & \mathbf{N}^{e-e'}_M \\ \mathbf{0} & \mathbf{I} & \mathbf{0} \end{bmatrix} \begin{Bmatrix} \lambda \\ \mathbf{x}^{\mathrm{LB}}_1 \\ \mathbf{x}^{\mathrm{LB}}_{24} \end{Bmatrix} = \begin{Bmatrix} \mathbf{0} \\ \mathbf{0} \\ \mathbf{0} \\ \mathbf{b} \end{Bmatrix} \\ \mathbf{x}^{\mathrm{LB}}_4, \quad \lambda \text{ free} \\ \mathbf{x}^{\mathrm{LB}}_{13} \in \underbrace{\mathscr{L}^3\times\cdots\times\mathscr{L}^3}_{3\times nele} \end{cases} \end{aligned} \tag{B7}$$

valid in Von Mises or Mohr–Coulomb plasticity with $\phi=0$. For each plastic model, the vector $\mathbf{b}$ is given by $\mathbf{b}^{\mathrm{T}}_{\mathrm{VM}}=2\sigma_Y/\sqrt{3}\{1\ldots1\}_{3\times nele}$ and $\mathbf{b}^{\mathrm{T}}_{\mathrm{MC}}=2c\{1\ldots1\}_{3\times nele}$, respectively. Matrices $\mathbf{A}_M$, $\mathbf{N}^g_M$ and $\mathbf{N}^{e-e'}_M$ are the assembling of the elemental products $\mathbf{A}^e\mathbf{M}$ and nodal products $\mathbf{N}^n\mathbf{M}$. The global vectors $\mathbf{x}^{\mathrm{LB}}_1$ and $\mathbf{x}^{\mathrm{LB}}_{24}$ have the following components $\mathbf{x}^{\mathrm{LB}\,\mathrm{T}}_1=\{x^{1,1\,\mathrm{T}}_1\ldots\mathbf{x}^{3,nele\,\mathrm{T}}_1\}_{3\times nele}$ and $\mathbf{x}^{\mathrm{LB}\,\mathrm{T}}_{24}=\{\mathbf{x}^{1,1}_{24}\ldots\mathbf{x}^{3,nele}_{24}\}_{3\times3\times nele}$.

DOI: 10.1002/nme

A slightly shorter expression than (B7) is obtained when inserting transformation (B6) into (B4), which gives rise to the lower bound optimization problem in Mohr–Coulomb plasticity with $\phi \neq 0$:

$$\begin{aligned} &\max \quad \lambda \\ &\text{s.t.} \quad \begin{cases} \begin{bmatrix} \mathbf{f} & \mathbf{A}_M \\ \mathbf{g} & \mathbf{N}_M^g \\ \mathbf{0} & \mathbf{N}_M^{e-e'} \end{bmatrix} \begin{Bmatrix} \lambda \\ \mathbf{x}_{13}^{\mathrm{LB}} \end{Bmatrix} = \begin{Bmatrix} -\mathbf{d}_{AM} \\ -\mathbf{d}_{NM} \\ \mathbf{0} \end{Bmatrix} \\ \lambda \text{ free} \\ \mathbf{x}_{13}^{\mathrm{LB}} \in \underbrace{\mathscr{L}^3 \times \cdots \times \mathscr{L}^3}_{3 \times nele} \end{cases} \end{aligned} \tag{B8}$$

where $\mathbf{d}_{AM}$ and $\mathbf{d}_{NM}$ are the assembling of the elemental products $\mathbf{A}^e\mathbf{M}_{\mathrm{MC}}\mathbf{d}$ and $\mathbf{N}^n\mathbf{M}_{\mathrm{MC}}\mathbf{d}$. The three-dimensional Lorentz cone $\mathscr{L}^3$ is defined as $\mathscr{L}^3 = \{\mathbf{x} \in \mathbb{R}^3 | x_1 \geqslant \sqrt{x_2^2 + x_3^2}\}$.

APPENDIX C: DISCRETE UPPER BOUND PROBLEM

Inserting the membership constraints for the edge traction $\mathbf{t}^{\mathrm{UB}}$, the optimization problem in (13b) turns into

$$\begin{aligned} &\max \quad \lambda \\ &\text{s.t.} \quad \begin{cases} a(\boldsymbol{\sigma}^{\mathrm{UB}}, \mathbf{u}^{\mathrm{UB}}) = \lambda \ell(\mathbf{u}^{\mathrm{UB}}), \quad \forall \mathbf{u}^{\mathrm{UB}} \in \mathscr{U}^{\mathrm{UB}} \\ \mathbf{t}^{\mathrm{UB}} \in \mathscr{B}_t^{\mathrm{UB}} \\ \boldsymbol{\sigma}^{\mathrm{UB}} \in \mathscr{B}^{\mathrm{UB}} \end{cases} \end{aligned} \tag{C1}$$

where $\boldsymbol{\sigma}^{\mathrm{UB}} = \{\boldsymbol{\sigma}^{1\mathrm{T}} \ldots \boldsymbol{\sigma}^{nele\mathrm{T}}\}_{3 \times nele}$ and $\mathbf{u}^{\mathrm{UB}} = \{\mathbf{u}^{1\mathrm{T}} \ldots \mathbf{u}^{nele\mathrm{T}}\}_{2 \times 3 \times nele}$ are the global vectors of stresses and velocities, respectively. Their elemental components are given by $\boldsymbol{\sigma}^e = \{\sigma_{xx}^e \ \sigma_{yy}^e \ \sigma_{xy}^e\}$ and $\mathbf{u}^{e\mathrm{T}} = \{\mathbf{u}^{1,e\mathrm{T}} \ \mathbf{u}^{2,e\mathrm{T}} \ \mathbf{u}^{3,e\mathrm{T}}\}$. In addition, we denote the nodal traction at the edge $\xi^{e-e'}$ by $\mathbf{t}^{e-e\mathrm{T}} = \{\mathbf{t}^{1,e-e'\mathrm{T}} \mathbf{t}^{2,e-e'\mathrm{T}}\}$. In order to recast (C1) in a standard optimization form, we first note that, recalling the nodal matrices $\mathbf{D}^n$ in (B2a), the elemental contribution of the terms in $a(,)$ and $\ell()$ may be expressed as

$$\begin{aligned} \sum_{e=1,nele} a(\boldsymbol{\sigma}^e, \mathbf{u}^e) &= \sum_{e=1,nele} \mathbf{u}^e \cdot \int_{\Omega^e} \begin{bmatrix} \mathbf{D}^1 \\ \mathbf{D}^2 \\ \mathbf{D}^3 \end{bmatrix} \mathrm{d}V \boldsymbol{\sigma}^e + \sum_{e,e' \in \xi^{e-e'}} \int_{\xi^{e-e'}} \mathbf{t}^{e-e'} (\mathbf{u}^e - \mathbf{u}^{e'}) \, \mathrm{d}\Gamma \\ &= \sum_{e=1,nele} \mathbf{u}^e \cdot \tilde{\mathbf{A}} \boldsymbol{\sigma}^e + \sum_{e,e' \in \xi^{e-e'}} \mathbf{u}^{e-e'} \cdot \mathbf{B}^e \mathbf{t}^{e-e'} \\ &= \mathbf{u}^{\mathrm{UB}} \cdot (\mathbf{A}\boldsymbol{\sigma}^{\mathrm{UB}} + \mathbf{B}\mathbf{t}) \end{aligned} \tag{C2}$$

DOI: 10.1002/nme

$$\sum_{e=1,nele}\int_{\Omega^e}\mathbf{u}^e\cdot\mathbf{f}\,\mathrm{d}V=\sum_{e=1,nele}\sum_{n=1,2,3}\mathbf{u}^{n,e}\cdot\int_{\Omega^e}I^n\mathbf{f}\,\mathrm{d}V=\sum_{e=1,nele}\mathbf{u}^e\cdot\mathbf{f}^e=\mathbf{u}^{\mathrm{UB}}\cdot\mathbf{f}$$

$$\sum_{e\in\Gamma_g}\int_{\Gamma_g^e}\mathbf{u}^e\cdot\mathbf{g}\,\mathrm{d}\Gamma=\sum_{e\in\Gamma_g}\sum_{n\in\Gamma_g^e}\mathbf{u}^{n,e}\cdot\int_{\Gamma_g^e}I^n\mathbf{g}\,\mathrm{d}\Gamma=\sum_{e\in\Gamma_g}\mathbf{u}^e\cdot\mathbf{g}^e=\mathbf{u}^{\mathrm{UB}}\cdot\mathbf{g}$$

where $\tilde{\mathbf{A}}^{\mathrm{e}^{\mathrm{T}}}=\int_{\Omega^e}[\mathbf{D}^{1^{\mathrm{T}}}\ \mathbf{D}^{2^{\mathrm{T}}}\ \mathbf{D}^{3^{\mathrm{T}}}]\,\mathrm{d}V$. The nodal velocities at the edges $\mathbf{v}_\xi^{e-e'}$ and the elemental matrix $\mathbf{B}^e$ are given by

$$\mathbf{u}_\xi^{e-e'}=\begin{Bmatrix}\mathbf{u}^{1,e}\\ \mathbf{u}^{2,e}\\ \mathbf{u}^{1,e'}\\ \mathbf{u}^{2,e'}\end{Bmatrix},\quad \mathbf{B}^{e-e'}=\begin{bmatrix}\tilde{\mathbf{I}}^{11} & \tilde{\mathbf{I}}^{12}\\ \tilde{\mathbf{I}}^{21} & \tilde{\mathbf{I}}^{22}\\ -\tilde{\mathbf{I}}^{11} & -\tilde{\mathbf{I}}^{12}\\ -\tilde{\mathbf{I}}^{21} & -\tilde{\mathbf{I}}^{22}\end{bmatrix},\quad \tilde{\mathbf{I}}^{ij}=I_\xi^i I_\xi^j\mathbf{I}_2$$

with $\mathbf{I}_2$ being the 2×2 unit matrix and $I_\xi^n, n=1,2$ the nodal interpolating functions at the edges. The elemental vectors $\mathbf{f}^e$ and $\mathbf{g}^e$ in (C2) are two elemental vectors associated with the body and surface loads. Matrices $\tilde{\mathbf{A}}$ and $\mathbf{B}$ and vectors $\mathbf{f}$ and $\mathbf{g}$ are the assembled elemental contributions of $\tilde{\mathbf{A}}^e$, $\mathbf{B}^{e-e'}$, $\mathbf{f}^e$ and $\mathbf{g}^e$, respectively.

With this notation at hand, the condition $a(\boldsymbol{\sigma}^{\mathrm{UB}},\mathbf{u}^{\mathrm{UB}})=\lambda\ell(\mathbf{u}^{\mathrm{UB}}),\ \forall\mathbf{u}^{\mathrm{UB}}\in\mathscr{U}^{\mathrm{UB}}$ is equivalent to the following system of equations:

$$\tilde{\mathbf{A}}\boldsymbol{\sigma}^{\mathrm{UB}}+\mathbf{B}\mathbf{t}^{\mathrm{UB}}-\lambda(\mathbf{f}+\mathbf{g})=\mathbf{0}$$

Consequently, we can rewrite the upper bound optimization problem in (C1) as

$$\begin{aligned}\max\quad & \lambda\\ \text{s.t.}\quad & \begin{cases}[-(\mathbf{f}+\mathbf{g})\ \ \mathbf{B}\ \ \tilde{\mathbf{A}}]\begin{Bmatrix}\lambda\\ \mathbf{t}^{\mathrm{UB}}\\ \boldsymbol{\sigma}^{\mathrm{UB}}\end{Bmatrix}=\mathbf{0}\\ \mathbf{t}^{\mathrm{UB}}\in\mathscr{B}_t^{\mathrm{UB}}\\ \boldsymbol{\sigma}^{\mathrm{UB}}\in\mathscr{B}^{\mathrm{UB}}\end{cases}\end{aligned}\tag{C3}$$

The membership constraints may be recasted as conic constraints by using the following transformations. Regarding the tractions, for each interior edge $\xi^{e-e'}$, the Von Mises condition in (16b) is applied to the two nodal tractions $\mathbf{t}^{1,e-e'}$ and $\mathbf{t}^{2,e-e'}$. After introducing the variable $\mathbf{z}^n=\{z_1^n\ z_2^n\}^{\mathrm{T}}$, with $z_2=t_T^n$, the Von Mises condition in (16b) is equivalent to

$$\begin{aligned}&\mathbf{z}^n\in\mathscr{L}^2,\quad n=1,2\\ &z_1^n=\sigma_Y/\sqrt{3},\quad n=1,2\\ &t_N^n\ \text{free},\quad n=1,2\end{aligned}\tag{C4a}$$

DOI: 10.1002/nme

The relation between the local components of the tractions $\{t_T^n t_N^n\}$ and the x–y components of $\mathbf{t}^{n,e-e'}$ for each node n at the edge $e-e'$ is given by the relation $\{t_T^n t_N^n\}=\mathbf{R}^{-1}\mathbf{t}^{n,e-e'}$, where $\mathbf{R}$ is the two-dimensional matrix that rotates the local edge axis $\xi^{e-e'}$ into the global x.

The Mohr–Coulomb condition in (16c) may be expressed in a manner similar to (C4a)

$$\mathbf{z}^n \in \mathscr{L}^2, \quad n=1,2 \tag{C4b}$$

where the following transformation of variables has been used:

$$\mathbf{z}^n = \begin{bmatrix} -\tan\phi & 0 \\ 0 & 1 \end{bmatrix} \begin{Bmatrix} t_N^{n,e-e'} \\ t_T^{n,e-e'} \end{Bmatrix} + \begin{Bmatrix} c \\ 0 \end{Bmatrix}, \quad n=1,2$$

For each internal edge $\xi^{e-e'}$, the inverse of this transformation may be expressed as

$$\mathbf{t}^{e-e'} = \begin{bmatrix} \mathbf{R} & \mathbf{0} \\ \mathbf{0} & \mathbf{R} \end{bmatrix} \left(\begin{bmatrix} -1/\tan\phi & 0 & 0 & 0 \\ 0 & 1 & 0 & 0 \\ 0 & 0 & -1/\tan\phi & 0 \\ 0 & 0 & 0 & 1 \end{bmatrix} \begin{Bmatrix} \mathbf{z}^1 \\ \mathbf{z}^2 \end{Bmatrix} + \frac{c}{\tan\phi} \begin{Bmatrix} 1 \\ 0 \\ 1 \\ 0 \end{Bmatrix} \right)$$

$$= \mathbf{R}^{e-e'}(\mathbf{T}^{e-e'}\mathbf{z}^{e-e'} + \mathbf{b}_{t\mathrm{MC}}^{e-e'})$$

In order to recast the stress membership constraint in (C3) as a conic constraint, we resort to the same technique employed in the lower bound method. In the present case, though, the stresses field is not nodal, but elemental, and thus we will use the transformations in (B3) but applied to the elemental stresses $\boldsymbol{\sigma}^e$. After gathering relations in (C3) and (C4a), the resulting optimization problem in Von Mises plasticity and purely frictional Mohr–Coulomb material ($\phi=0$) reads

$$\begin{aligned} &\sup \quad \lambda \\ &\text{s.t.} \quad \begin{cases} \begin{bmatrix} -(\mathbf{f}+\mathbf{g}) & (\mathbf{BR})_N & (\mathbf{BR})_T & \mathbf{0} & \mathbf{0} & \tilde{\mathbf{A}}_M \\ \mathbf{0} & \mathbf{0} & \mathbf{0} & \mathbf{0} & \mathbf{I} & \mathbf{0} \\ \mathbf{0} & \mathbf{0} & \mathbf{0} & \mathbf{I} & \mathbf{0} & \mathbf{0} \end{bmatrix} \begin{Bmatrix} \lambda \\ \mathbf{t}_N^{\mathrm{UB}} \\ \mathbf{z}_2^{\mathrm{UB}} \\ \mathbf{z}_1^{\mathrm{UB}} \\ \mathbf{x}_1^{\mathrm{UB}} \\ \mathbf{x}_{24}^{\mathrm{UB}} \end{Bmatrix} = \begin{Bmatrix} -\mathbf{b}_t \\ \mathbf{b} \\ \frac{1}{2}\mathbf{b} \end{Bmatrix} \\ \lambda, \mathbf{t}_N^{\mathrm{UB}}, \mathbf{x}_4^{\mathrm{UB}} \text{ free} \\ \mathbf{z}^{\mathrm{UB}} \in \underbrace{\mathscr{L}^2 \times \cdots \times \mathscr{L}^2}_{2\times N_I} \\ \mathbf{x}_{13}^{\mathrm{UB}} \in \underbrace{\mathscr{L}^3 \times \cdots \times \mathscr{L}^3}_{3\times nele} \end{cases} \end{aligned} \tag{C5a}$$

where N_I is the number of interior edges, and the vector $\mathbf{b}$ is given by $\mathbf{b}_{\mathrm{VM}}^{\mathrm{T}}=2\sigma_Y/\sqrt{3}\{1\ \ldots\ 1\}_{nele}$ and $\mathbf{b}_{\mathrm{MC}}^{\mathrm{T}}=2c\{1\ \ldots\ 1\}_{nele}$ in Von Mises and Mohr–Coulomb plasticity, respectively. Matrices

DOI: 10.1002/nme

$(\mathbf{BR})_N$ and $(\mathbf{BR})_T$ are the assembled terms of the product $\mathbf{B}^{e-e'}\mathbf{R}^{e-e'}$ associated with variables t_N and t_T, respectively. Vector $\mathbf{t}_N$ contains all the nodal normal components t_N^n. In a Mohr–Coulomb material with $\phi \neq 0$, we obtain from Equations (C3) and (C4b),

$$\begin{aligned} &\sup \quad \lambda \\ &\text{s.t.} \quad \begin{cases} [-(\mathbf{f}+\mathbf{g}) \;\; \mathbf{BTR} \;\; \tilde{\mathbf{A}}_M] \begin{Bmatrix} \lambda \\ \mathbf{z}^{\mathrm{UB}} \\ \mathbf{x}_{13}^{\mathrm{UB}} \end{Bmatrix} = -\mathbf{d}_{AM} - \mathbf{b}_t \\ \lambda \text{ free} \\ \mathbf{z} \in \underbrace{\mathscr{L}^2 \times \cdots \times \mathscr{L}^2}_{2 \times N_I} \\ \mathbf{x}_{13}^{\mathrm{UB}} \in \underbrace{\mathscr{L}^3 \times \cdots \times \mathscr{L}^3}_{3 \times nele} \end{cases} \end{aligned} \tag{C5b}$$

Matrix $\tilde{\mathbf{A}}_M$ and vector $\mathbf{d}_{AM}$ are the assembling of the elemental contributions $\tilde{\mathbf{A}}^e\mathbf{M}$ and $\mathbf{Md}$, with $\mathbf{M}$ and $\mathbf{d}$ in (A5b) and (A4b). The matrix product $\mathbf{BTR}$ is the assembled form of the elemental products $\mathbf{B}^{e-e'}\mathbf{T}^{e-e'}\mathbf{R}^{e-e'}$, and vector $\mathbf{b}_t$ is the assembling of the terms $\mathbf{B}^{e-e'}\mathbf{T}^{e-e'}\mathbf{R}^{e-e'}\mathbf{b}_{t\mathrm{MC}}^{e-e'}$.

APPENDIX D: DEDUCTION OF ELEMENTAL AND EDGE GAP CONTRIBUTIONS

Let us first note that, due to the equilibrium conditions at the Neumann and interior edges in (11), the following relation can be derived:

$$\begin{aligned} \sum_{e=1}^{nele} \int_{\partial\Omega^e} \boldsymbol{\sigma}^{\mathrm{LB}}\mathbf{n}\cdot\mathbf{u}^{\mathrm{UB}} \, \mathrm{d}\Gamma &= \lambda^{\mathrm{LB}} \sum_{\xi^N} \int_{\partial\Omega^e} \mathbf{g}\cdot\mathbf{u}^{\mathrm{UB}} \, \mathrm{d}\Gamma + \sum_{\xi^{e-e'}=1}^{N_I} \int_{\xi^{e-e'}} \boldsymbol{\sigma}^{\mathrm{LB}}\mathbf{n}\cdot[\![\mathbf{u}^{\mathrm{UB}}]\!] \, \mathrm{d}\Gamma \\ &= \lambda^{\mathrm{LB}} \int_{\partial\Omega} \mathbf{g}\cdot\mathbf{u}^{\mathrm{UB}} \, \mathrm{d}\Gamma + \sum_{\xi^{e-e'}=1}^{N_I} \int_{\xi^{e-e'}} \boldsymbol{\sigma}^{\mathrm{LB}}\mathbf{n}\cdot[\![\mathbf{u}^{\mathrm{UB}}]\!] \, \mathrm{d}\Gamma \end{aligned}$$

By using this relation, and from the condition $\ell(\mathbf{u}^{\mathrm{UB}}) = 1$, we can express the lower bound λ^{LB} as follows:

$$\begin{aligned} \lambda^{\mathrm{LB}} &= \lambda^{\mathrm{LB}}\ell(\mathbf{u}^{\mathrm{UB}}) = \lambda^{\mathrm{LB}} \int_\Omega \mathbf{f}\cdot\mathbf{u}^{\mathrm{UB}} \, \mathrm{d}V + \lambda^{\mathrm{LB}} \int_{\Gamma_g} \mathbf{g}\cdot\mathbf{u}^{\mathrm{UB}} \, \mathrm{d}\Gamma \\ &= \sum_{e=1}^{nele} \left(\int_{\Omega^e} (-\nabla\cdot\boldsymbol{\sigma}^{\mathrm{LB}})\cdot\mathbf{u}^{\mathrm{UB}} \, \mathrm{d}V + \int_{\partial\Omega^e} \boldsymbol{\sigma}^{\mathrm{LB}}\mathbf{n}\cdot\mathbf{u}^{\mathrm{UB}} \, \mathrm{d}\Gamma \right) \\ &\quad - \sum_{\xi^{e-e'}=1}^{N_I} \int_{\xi^{e-e'}} \boldsymbol{\sigma}^{\mathrm{LB}}\mathbf{n}\cdot[\![\mathbf{u}^{\mathrm{UB}}]\!] \, \mathrm{d}\Gamma \end{aligned} \tag{D1}$$

DOI: 10.1002/nme

On the other hand, the upper bound λ^{UB} is the solution of the min–max problem in (13a). From the expression of $a(,)$ in (14), we see that the inner maximum is equal to $+\infty$ if $\boldsymbol{\varepsilon} \neq \gamma \partial f / \partial \boldsymbol{\sigma}$ and $[\![\mathbf{u}^{\mathrm{UB}}]\!] \neq \gamma \partial f_t / \partial \mathbf{t}$, or equal to $D(\mathbf{u}^{\mathrm{UB}})$ otherwise. For Von Mises and Mohr–Coulomb plasticity, the rate of plastic dissipation at the optimum, and therefore also λ^{UB}, may be expressed as

$$\lambda^{\mathrm{UB}} = D(\mathbf{u}^{\mathrm{UB}})_{\mathrm{VM}} = \sum_{e=1}^{nele} \int_{\Omega^e} \sigma_Y \varepsilon_{\mathrm{eq}} \, \mathrm{d}V + \sum_{\xi^{e-e'}=1}^{N_I} \int_{\xi^{e-e'}} \frac{\sigma_Y}{\sqrt{3}} |[\![\mathbf{u}^{\mathrm{UB}}]\!]| \, \mathrm{d}\Gamma$$

$$\lambda^{\mathrm{UB}} = D(\mathbf{u}^{\mathrm{UB}})_{\mathrm{MC}} = \sum_{e=1}^{nele} \int_{\Omega^e} c \sqrt{\frac{3}{1+2\tan^2\phi}} \varepsilon_{\mathrm{eq}} \, \mathrm{d}V + \sum_{\xi^{e-e'}=1}^{N_I} \int_{\xi^{e-e'}} c \, \cos\phi |[\![\mathbf{u}^{\mathrm{UB}}]\!]| \, \mathrm{d}\Gamma$$

From these expressions, and (D1), the global gap $\lambda^{\mathrm{UB}} - \lambda^{\mathrm{LB}}$ may be expressed as the sum of elemental and edge contributions

$$\lambda^{\mathrm{UB}} - \lambda^{\mathrm{LB}} = \sum_{e=1}^{nele} \Delta_\lambda^e + \sum_{\xi^{e-e'}=1}^{N_I} \Delta_\lambda^\xi$$

where after setting $\mathbf{s}^{\mathrm{UB}} = -[\![\mathbf{u}^{\mathrm{UB}}]\!] / |[\![\mathbf{u}^{\mathrm{UB}}]\!]|$, each elemental and edge contribution reads, in Von Mises plasticity,

$$\Delta_\lambda^e = \int_{\Omega^e} (\sigma_Y \varepsilon_{\mathrm{eq}} + \nabla \cdot \boldsymbol{\sigma}^{\mathrm{LB}} \cdot \mathbf{u}^{\mathrm{UB}}) \, \mathrm{d}V - \int_{\partial\Omega^e} \boldsymbol{\sigma}^{\mathrm{LB}} \mathbf{n} \cdot \mathbf{u}^{\mathrm{UB}} \, \mathrm{d}\Gamma$$

$$\Delta_\lambda^\xi = \int_{\xi^{e-e'}} \left(\frac{\sigma_Y}{\sqrt{3}} - \boldsymbol{\sigma}^{\mathrm{LB}} \mathbf{n} \cdot \mathbf{s}^{\mathrm{UB}} \right) |[\![\mathbf{u}^{\mathrm{UB}}]\!]| \, \mathrm{d}\Gamma$$

and in Mohr–Coulomb,

$$\Delta_\lambda^e = \int_{\Omega^e} \left(c \sqrt{\frac{3}{1+2\tan^2\phi}} \varepsilon_{\mathrm{eq}} + \nabla \cdot \boldsymbol{\sigma}^{\mathrm{LB}} \cdot \mathbf{u}^{\mathrm{UB}} \right) \mathrm{d}V - \int_{\partial\Omega^e} \boldsymbol{\sigma}^{\mathrm{LB}} \mathbf{n} \cdot \mathbf{u}^{\mathrm{UB}} \, \mathrm{d}\Gamma$$

$$\Delta_\lambda^\xi = \int_{\xi^{e-e'}} (c \cos\phi - \boldsymbol{\sigma}^{\mathrm{LB}} \mathbf{n} \cdot \mathbf{s}^{\mathrm{UB}}) |[\![\mathbf{u}^{\mathrm{UB}}]\!]| \, \mathrm{d}\Gamma$$

ACKNOWLEDGEMENTS

This work has been financially supported by the Spanish Ministry of Education and Science (MEC), under the research program *Juan de la Cierva* and the grant BIA2007-66965. This support is greatly acknowledged.

REFERENCES

1. Chen WF. *Limit Analysis and Soil Plasticity*. Developments in Geotechnical Engineering, vol. 7. Elsevier: Amsterdam, 1975.
2. Christiansen E. Limit analysis of collapse states. *Handbook of Numerical Analysis*, Chapter II, vol. IV. North-Holland: Amsterdam, 1996; 193–312.

DOI: 10.1002/nme

3. Belytschko T, Hodge PG. Plane stress limit analysis by finite elements. *Journal of Engineering Mechanics* 1970; **96**:931–944.
4. Lysmer J. Limit analysis of plane problems in soil mechanics. *Journal of Soil Mechanics and Foundations Division* 1970; **96**:1311–1334.
5. Borges L, Zouain N, Costa N, Feijóo R. An adaptive approach to limit analysis. *International Journal of Solids and Structures* 2001; **38**:1707–1720.
6. Krabbenhøft K, Damkilde L. A general non-linear optimization algorithm for lower bound limit analysis. *International Journal for Numerical Methods in Engineering* 2003; **56**:165–184.
7. Lyamin AV, Sloan SW. Lower bound limit analysis using non-linear programming. *International Journal for Numerical Methods in Engineering* 2002; **55**:576–611.
8. Makrodimopoulos A, Martin CM. Lower bound limit analysis of cohesive-frictional materials using second-order cone programming. *International Journal for Numerical Methods in Engineering* 2006; **66**:604–634.
9. Ciria H. Computation of upper and lower bounds in limit state analysis using second-order cone programming and mesh adaptivity. *Ph.D. Thesis*, Department of Aeronomics and Astronomy, MIT, U.S.A., 2004.
10. Ciria H, Peraire J, Bonet J. Mesh adaptive computation of upper and lower bounds in limit analysis. *International Journal for Numerical Methods in Engineering*, DOI: 10.1002/nme.2275.
11. Díaz JN. Análisis en estado límite para suelos: cálculo de cotas exactas empleando el modelo Mohr–Coulomb mediante programación cónica de segundo orden. *Ph.D. Thesis*, ETSCCP, 2005.
12. Gutiérrez R. Evaluación de cotas estrictas para el análisis en estado límite de geomateriales mediante programación cónica de segundo orden. *Ph.D. Thesis*, ETSCCP, 2005.
13. Sloan SW, Kleeman PW. Upper bound limit analysis using discontinuous velocity fields. *Computer Methods in Applied Mechanics and Engineering* 1995; **127**(5):293–314.
14. Sturm JF. Using SeDuMi 1.02, a MATLAB toolbox for optimization over symmetric cones over symmetric cones. *Optimization Methods and Software* 1999; **11–12**:625–653. Available from: http://sedumi.mcmaster.ca.
15. Tütüncü RH, Toh KC, Todd MJ. Solving semidefinite–quadratic–linear programs using SDPT3. *Mathematical Programming Series B* 2003; **95**:189–217. Available from: http://www.math.nus.edu.sg/ mattohkc/sdpt3.html.
16. MOSEK ApS. The MOSEK optimization tools version 3.2 (Revision 8). *User's Manual and Reference*, 2005. Available from: http://www.mosek.com.
17. Lyamin AV, Sloan SW. Upper bound limit analysis using linear finite elements and non-linear programming. *International Journal for Numerical and Analytical Methods in Geomechanics* 2002; **26**:181–216.
18. Lyamin AV, Sloan, Krabbenhøft K, Hjiaj M. Lower bound limit analysis with adaptive remeshing. *International Journal for Numerical Methods in Engineering* 2005; **63**:1961–1974.
19. Christiansen E, Andersen KD. Computation of collapse states with Von Mises type yield condition. *International Journal for Numerical Methods in Engineering* 1999; **46**:1185–1202.
20. Christiansen E, Pedersen OS. Automatic mesh refinement in limit analysis. *International Journal for Numerical Methods in Engineering* 2001; **50**:1331–1346.
21. Krabbenhøft K, Lyamin AV, Sloan SW. Three-dimensional Mohr–Coulomb limit analysis using semidefinite programming. *Communications in Numerical Methods in Engineering*, DOI: 10.1002/cnm.1018.
22. Lyamin AV, Krabbenhøft K, Sloan SW, Hjiaj M. An adaptive algorithm for upper bound limit analysis using discontinuous velocity fields. *Proceedings of European Congress on Computational Methods in Applied Sciences and Engineering*, *ECCOMAS 2004*, Jyväskylä, Finland, 24–28 July 2004.
23. Krabbenhøft K, Lyamin AV, Hjiaj M, Sloan SW. A new discontinuous upper bound limit analysis formulation. *International Journal for Numerical Methods in Engineering* 2005; **63**:1069–1088.
24. Zouain N, Borges LA, Silveira JL. An algorithm for shakedown analysis with nonlinear yield functions. *Computer Methods in Applied Mechanics and Engineering* 2002; **191**:2463–2481.
25. Ekeland I, Témam R. *Convex Analysis and Variational Problems*. SIAM: Philadelphia, PA, 1999.
26. Prandtl L. Über die härte plastischer körper. *Nachrichten von der Gesellshaft der Wissenshaften zu Gottingen Mathematisch-physikalische Klasse* 1920; **9**:302–325.
27. Díez P, Huerta A. A unified approach to remeshing strategies for finite element h-adaptivity. *Computer Methods in Applied Mechanics and Engineering* 1999; **176**:215–229.
28. Roca X, Sarrate J. Management, design and development of a mesh generation environment using open source software. *Proceedings of the 17th International Meshing Roundtable*, 2007.
29. Liu Y, Zhang X, Cen Z. Numerical determination of limit loads for three-dimensional structures using boundary element method. *European Journal of Mechanics A/Solids* 2004; **23**:129–138.
30. Díez P, Arroyo M, Huerta A. Adaptivity based on error estimation for viscoplastic softening materials. *Mechanics of Cohesive-Frictional Materials* 2000; **5**:87–112.

DOI: 10.1002/nme